ADVANCED HEALTHCARE MATERIALS
www.advhealthmat.de

Ligand-Selective Targeting of Macrophage Hydrogel Elicits Bone Immune-Stem Cell Endogenous Self-Healing Program to Promote Bone Regeneration

Jiahao Wang, Liang Zhang, Lingjun Wang, Jincheng Tang, Wei Wang, Yichang Xu, Ziang Li, Zhouye Ding, Xinzhao Jiang, Kun Xi, Liang Chen,* and Yong Gu**

Targeting macrophages can facilitate the site-specific repair of critical bone defects. Herein, a composite hydrogel, gelatin-*Bletilla striata* polysaccharide-mesoporous bioactive glass hydrogel (GBM^{gel}), is constructed via the self-assembly of mesoporous bioactive glass on polysaccharide structures, through the Schiff base reaction. GBM^{gel} can efficiently capture macrophages and drive the recruitment of seed stem cells and vascular budding required for regeneration in the early stages of bone injury, and the observed sustained release of inorganic silicon ions further enhances bone matrix deposition, mineralization, and vascular maturation. Moreover, the use of macrophage-depleted rat calvarial defect models further confirms that GBM^{gel}, with ligand-selective macrophage targeting, increases the bone regeneration area and the proportion of mature bone. Mechanistic studies reveal that GBM^{gel} upregulates the TLR4/NF-κB and MAPK macrophage pathways in the early stages and the JAK/STAT3 pathway in the later stages; thus initiating macrophage polarization at different time points. In conclusion, this study is based on the endogenous self-healing properties of bone macrophages, which enhances stem cell homing, and provides a research and theoretical basis upon which bone tissue can be reshaped and regenerated using the body's immune power, providing a new strategy for the treatment of critical bone defects.

1. Introduction

Severe trauma often results in critical bone defects.[1] However, a bone defect that exceeds the critical range of the innate self-healing capacity of a tissue can result in chronic inflammation at the injury site, with the delay in repair persisting sometimes over an entire lifetime.[2] Macrophages play a pivotal role in the immune response that leads to endogenous self-healing,[3] and are thought to exhibit various phenotypes following such an injury. The "classically activated" M1 macrophages are known for their proinflammatory cytokine production and the "alternatively activated" M2 macrophages release anti-inflammatory factors.[4] Both M1 and M2 macrophages are indispensable for the self-healing of bone, and the targeted and timely regulation of these macrophages can promote healing.[5] Currently, biomaterials that improve conditions by carrying exogenous cytokines or cells are used to heal bone injuries, and the important role of immune cells that initiate endogenous self-healing at critical bone defects is generally overlooked.[6]

In recent years, biomaterials with precisely controlled structures have been widely studied for drug delivery and new tissue regeneration,[7] and the developed cell-free material strategies for the timed and targeted regulation of endogenous bone repair programs are particularly conducive to fracture healing.[8] The extracellular matrix (ECM)-like characteristics of hydrogels means that they can promote cell migration and adhesion, and these materials have thus been widely used as biomaterials.[9] Given the uniqueness of critical bone defects, hydrogels that are formed by Schiff base reactions have the advantage of in situ gelation and self-healing properties, rendering them suitable for filling bone defects of various shape.[10] Moreover, the excellent biocompatibility and degradability of gelatin-based hydrogels renders them nontoxic to the human body.[11] Our previous research showed that dextran (DEX) structures can form hydrogels by binding with the amino groups in gelatin, and can effectively adhere to fragmented bone pieces and guide bone healing through degradation.[12] However, DEX-based hydrogels lack

J. Wang, L. Wang, J. Tang, W. Wang, Y. Xu, Z. Li, Z. Ding, X. Jiang, K. Xi, L. Chen, Y. Gu
Department of Orthopedics
the First Affiliated Hospital of Soochow University
188 Shizi Road, Gusu District, Suzhou, Jiangsu 215006, P. R. China
E-mail: xikun@suda.edu.cn; chenliang7737@suda.edu.cn; guyong1019@suda.edu.cn
L. Zhang
Department of Orthopedics
Beijing Friendship Hospital
Capital Medical University
No. 95, Yong An Road, XiCheng District, Beijing 100050, P. R. China
The ORCID identification number(s) for the author(s) of this article can be found under https://doi.org/10.1002/adhm.202303851

DOI: 10.1002/adhm.202303851

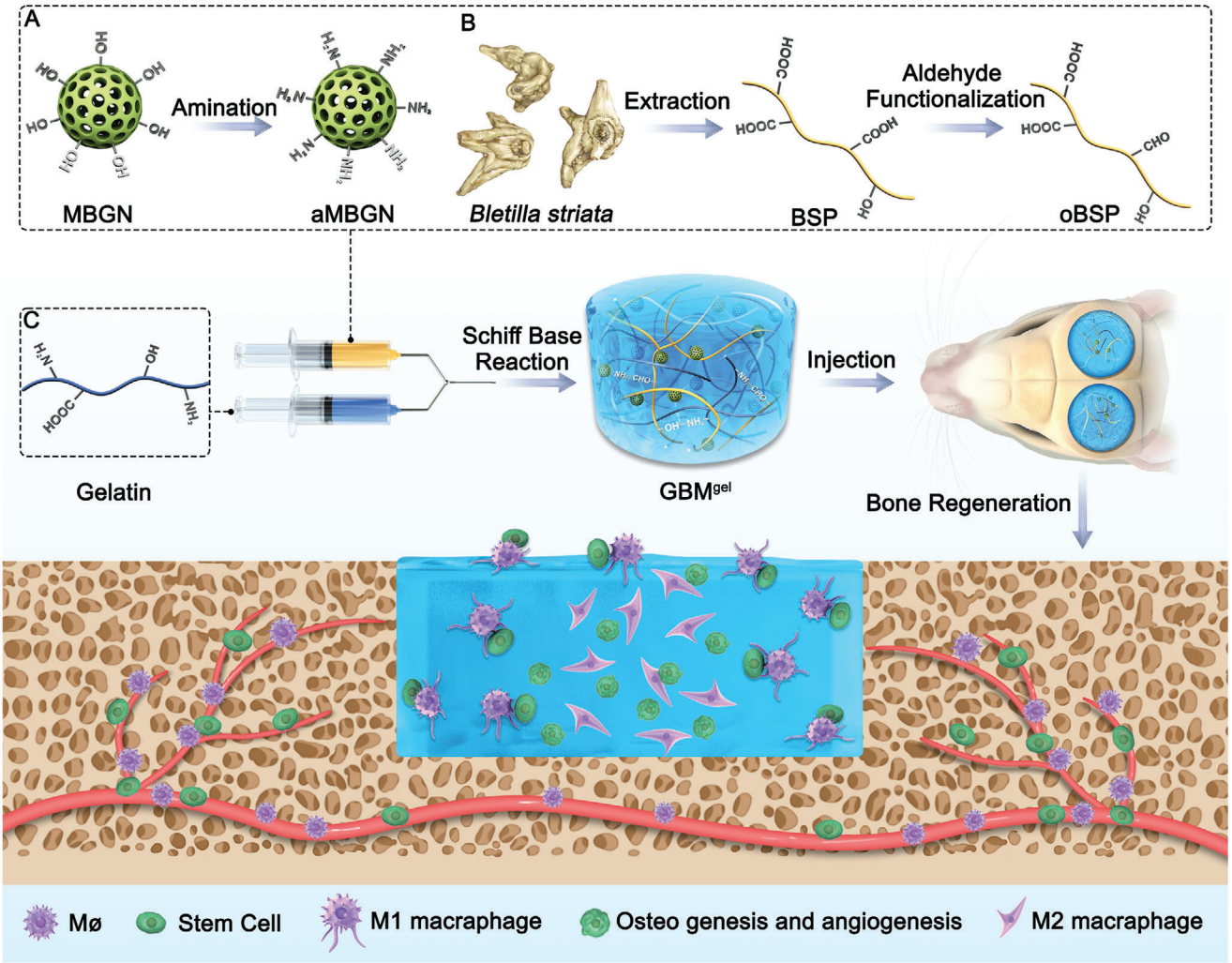

Scheme 1. Schematic illustration of the construction and application of the inorganic–organic double-cross-linked hydrogel for augmented bone regeneration. The GBM^{gel} comprises aMBGN, oBSP, and gelatin. When the GBM^{gel} is applied to the bone defect, it targets macrophages, initiating a brief inflammatory response that is then controlled, thus inducing the bone immune-stem cell endogenous self-healing program.

immunomodulatory properties and do not stimulate endogenous self-healing via bone immune-stem cells. Polysaccharides such as *Bletilla striata* polysaccharide (BSP, comprising repeating mannose and glucose units), which is extracted from the roots of the East Asian plant Isatis, have gained significant attention due to their cell-specific targeting properties.[13] BSP has excellent biocompatibility and biodegradability, is inexpensive, and has been shown to promote wound healing, with anti-inflammatory and antifibrotic properties, and can be applied in medical materials such as hydrogels, sponges, and microneedles.[14] Therefore, combining BSP with gelatin-based hydrogels would maximize the immunoregulatory and bone-promoting characteristics while filling bone defects. Such a composite hydrogel would offer superior performance, providing a comprehensive solution for repairing critical bone defects while simultaneously promoting bone healing and regeneration, and the introduction of mesoporous bioactive glass (MBGN), an inorganic material in the calcium-silicon-phosphate family that promotes macrophage polarization toward the M2 phenotype, enhancing osteogenesis; it would likely improve the gel even further.[15] The rich mesoporous structure of MBGN would aid in its dispersion and adhesion within a hydrogel, enhancing its overall biological and mechanical properties.[16] MBGN particles can be recognized by the endogenous macrophages that are mobilized in the hydrogel; thus, MBGN can play a continuous role in attracting intervening macrophages throughout the healing process.[17]

In this study, a bone tissue engineering treatment strategy that cross-links aminosilane-modified mesoporous bioactive glass (aMBGN) with aldehyde-functionalized *B. striata* polysaccharide (oBSP) and gelatin through the Schiff base reaction (**Scheme 1**) was established. The treatment initiates natural bone defect repair by mimicking innate immunity, sequentially mobilizing immune-stem cells, and triggering the endogenous bone repair program. Macrophages are recruited to the hydrogel, where they are reprogrammed to the M1 type in the early stage, releasing related factors that recruit endogenous stem cells and provide an

early osteogenesis and angiogenesis matrix. Endogenous stem cells then enter the defect along the hydrogel filling within the critical bone defect. As the MBGN particles in the hydrogel are recognized and endocytosed by macrophages, the macrophages are polarized to the M2 type, controlling the inflammation and releasing related factors into the chemotaxis stem cells for osteogenesis and angiogenesis. Evaluation of the biological mechanisms by which the composite scaffold regulates immune osteogenesis was performed by protein transcriptomic analysis and investigation of the related signaling pathways, and the efficacy of the GBM^{gel}, which selectively targets macrophages and stimulates the endogenous self-healing program of the immune-stem cells in the bone to promote healing, was further validated in a critical cranial bone defect rat model through liposome-mediated macrophage depletion. The results proved that following a critical bone defect, filling it with GBM^{gel} via in situ injection leads to targeting and reprogramming of the macrophages, initiating brief and acute inflammation that is controlled in a timely manner, and inducing the immune-stem cell endogenous self-healing program to promote bone regeneration.

2. Results and Discussion

2.1. Preparation and Characterization of Hydrogel

The aim of this study was to create a GBM^{gel} loaded with BSP and MBGN for the treatment of critical bone defects. The GBM^{gel} was designed to self-assemble in situ at the site of a bone defect, providing an applicable cellular microenvironment for the promotion of bone-defect regeneration through immunomodulation.

BSP, known for its high biocompatibility and affinity for macrophages, was further modified through aldehyde functionalization, resulting in oBSP.[18] MBGN was prepared based on a previously reported procedure and further modified by amination to obtain aMBGN.[19] The successful synthesis of the oBSP and aMBGN was confirmed by Fourier transform infrared spectroscopy (FT-IR) (Figure S1A, Supporting Information),[20] with results showing a peak at 1730 cm^{-1} following oxidation of the polysaccharide, which indicated the presence of reactive aldehyde groups on the polysaccharide molecular chain that could be utilized in subsequent experiments. Additionally, after modification with aminopropyltriethoxysil-ane (APTES), a peak at 3420 cm^{-1} in the FT-IR spectrum of MBGN confirmed the presence of amino groups on the MBGN, which could also be employed (Figure S1B, Supporting Information).

Observations of synthetic MBGN through scanning electron microscopy (SEM) and transmission electron microscopy (TEM) revealed a smooth spherical shape with a uniform size distribution (Figure S2A,B, Supporting Information). No differences were observed in the morphologies or distributions of aMBGN and MBGN. Dynamic light scattering results indicated an average diameter of ≈221.3 ± 24.6 nm for aMBGN, with a low polydispersity index of 0.0532 (Figure S2C, Supporting Information), suggesting relatively narrow size distribution and uniformity for the aMBGN particles. Furthermore, broad diffraction peaks over the range 15°–30° in the X-ray diffraction (XRD) spectrum of MBGN (Figure S2D, Supporting Information) are characteristic of amorphous bioactive glass,[21] confirming the amorphous nature of the MBGN.

The SEM results indicate that the average pore size of ≈115 µm for the hydrogel remains relatively unchanged under the addition of aMBGN (**Figure 1A**). However, the pore structure is denser, and irregularities with noticeable spherical protrusions can be observed on the hydrogel surface. It is generally recognized that a pore size of around 100 µm is conducive to promoting cell migration and tissue ingrowth, while uneven surfaces facilitate cell adhesion.[22] The energy-dispersive spectroscopy spectrum (EDS) of GBM^{gel} also revealed the additional presence of calcium (Ca) and silicon (Si) in the structure, confirming the incorporation of MBGN within the hydrogel. Phosphorus (P) was not observed, which may be because the P content is very low in MBGN (Figure 1B,C). This structural integration is essential for the intended functions and interactions of the hydrogel with the target cells and tissues.

To produce the required hydrogel, aMBGN was first mixed with oBSP solution followed by a gelatin solution of equal concentration. These components form hydrogels via Schiff and hydrogen bonds. Observation of the hydrogel containing aMBGN indicated noticeable turbidity (Figure 1D). Additionally, the gelation time was significantly shortened compared to that observed in the GB^{gel} group to which no aMBGN was added. The GB^{gel} group required 10 min for gelation, whereas the GBM^{gel} group with aMBGN required only 3 min. This accelerated gelation is beneficial for preventing the loss of hydrogel liquid during in situ injection, which can occur when gelation occurs over excessive periods.[23] Absorption peaks at 1630 cm^{-1} in the FT-IR spectra of GBM^{gel} indicate the presence of Schiff base bonds that have formed via reactions between the main gelatin chain, the —NH2 groups on the aMBGN, and the C═O groups on the oBSP. Meanwhile, two new peaks at ≈883 and 1028 cm^{-1} in the FT-IR spectra obtained for the GBM^{gel} are attributed to Si—O—Si bending and stretching vibrations in the silicate glass, confirming the presence of MBGN within the GBM^{gel} (Figure 1E).

Rheological tests were used to evaluate the frequency sweep of the hydrogels by comparing both groups at oscillation frequencies of 0–12.5 Hz. The results indicated a higher storage modulus (*G'*) than loss modulus (*G''*) in both groups, indicating the formation of an elastic network within the hydrogels (Figure 1F). Furthermore, the higher *G'* for the GBM^{gel} group compared to that of the GBM^{gel} suggest superior applicability, which is potentially attributed to the MBGN loading. The results of strain sweep on the two hydrogel groups showed no particular change in the storage modulus of either group as the shear strain was increased, until the critical shear strain was reached, at which point, the storage and loss modulus intersected before dropping rapidly, indicating destruction of the 3D network.[24] The critical strain 191.3% for the GBM^{gel} is significantly higher than the 111.7% that was obtained for the GB^{gel}, indicating that MBGN improves the strain tolerance of the hydrogel (Figure 1G). This may be related to the dispersion of MBGN and the Schiff base bonds within the hydrogel. Additionally, good injectability properties are required because the hydrogels injected in situ into irregular critical bone defects.[25] Injection of the fully gelled GBM^{gel} into a vial containing phosphate-buffered saline (PBS) solution (Figure 1H) indicated that the GBM^{gel} retained its complete structure in the PBS, suggesting that GBM^{gel} can be injected. Simultaneously, the results of shear viscosity testing show that the viscosity of the GBM^{gel} decreases as the rotation

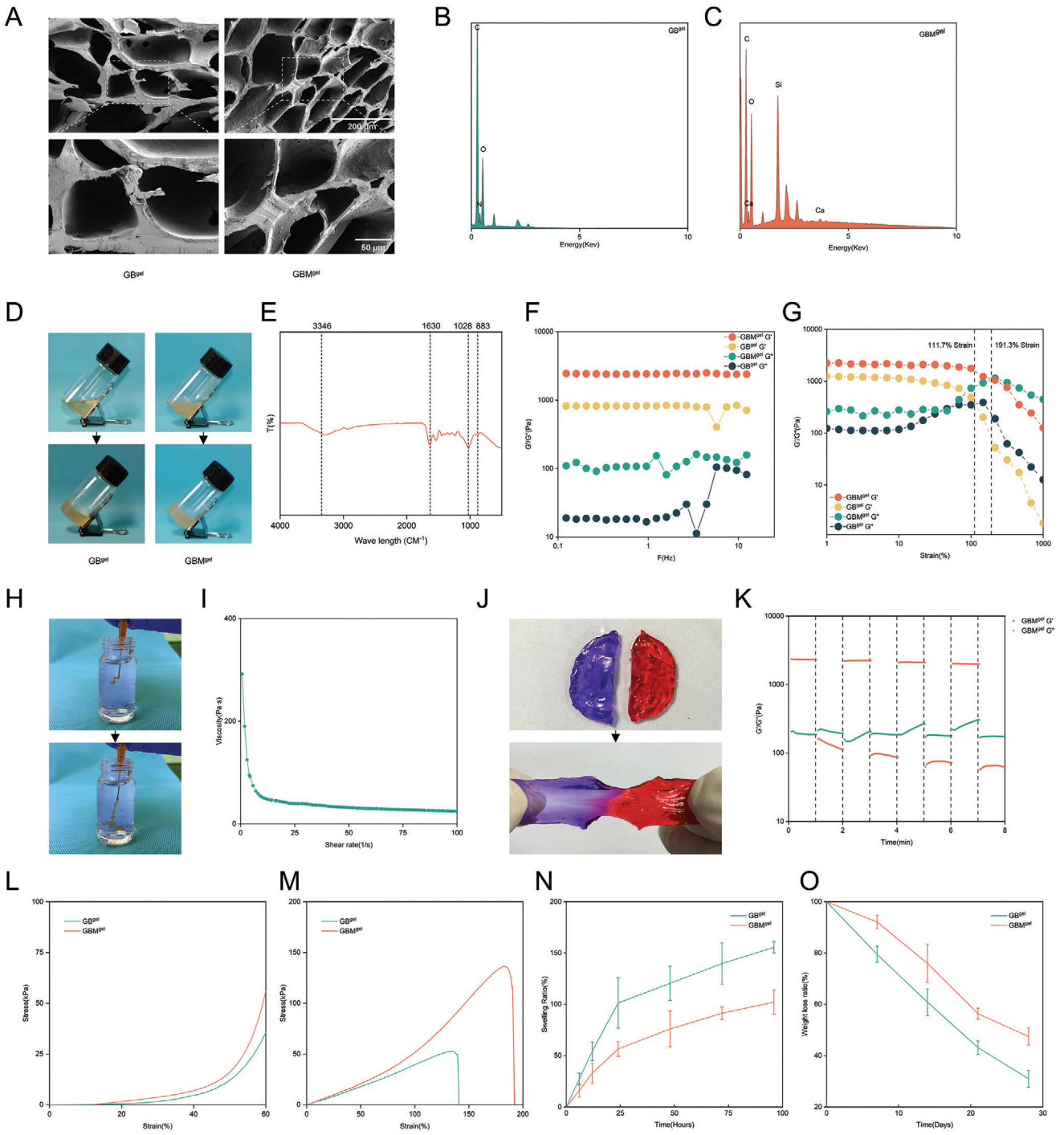

Figure 1. Hydrogel characterization. A) SEM images of GB^{gel} and GBM^{gel}. B) EDS profile of elements in GB^{gel} and C) GBM^{gel}. D) Images showing sol–gel transition in the hydrogels. E) FT-IR spectra of GBM^{gel}. F) Frequency sweep of GB^{gel} and GBM^{gel} from 0.1 to 12.5 Hz at 5% strain. G) Strain sweep of GB^{gel} and GBM^{gel} from 1% to 1000% at 1 Hz. H) Injection of gelled GBM^{gel} into PBS to verify injectability. I) Shear viscosity of GBM^{gel}. J) Images showing the self-healing properties of GBM^{gel}. K) Step strain testing of GBM^{gel} at alternating strains of 1% and 400%. L) Compression testing of GB^{gel} and GBM^{gel}. M) Tensile testing of GB^{gel} and GBM^{gel}. N) Swelling curves for GB^{gel} and GBM^{gel}. O) Degradation curves for GB^{gel} and GBM^{gel}. (Data presented as mean ± standard deviation, $n = 3$).

speed increases, further proving the good injectability of the GBM^{gel} (Figure 1I). It is difficult to avoid deformation in hydrogel that has been used to fill critical bone defects due to patient movement. However, hydrogels with Schiff base bonds can spontaneously repair through the action of reversible covalent bonds, preventing the hydrogel from being squeezed out of the defect.[26] To test this process, two complete GBM^{gel} portions were cut in half and placed together, with results showing that the two hydrogels healed after 5 min, indicating the self-healing properties of the GBM^{gel} (Figure 1J). Step strain testing showed that rapidly increasing the stress to 400%, exceeding the critical strain value of GBM^{gel}, instantly decreases the G' value of the GBM^{gel} to $< G''$, indicating that the hydrogel was destroyed and that the gel changed from a solid to a liquid state. Converting the stress to low strain results in an increase in the G' value of the hydrogel to $> G''$, indicating that the hydrogel has restored its original gel state, proving the self-healing properties of GBM^{gel} (Figure 1K).

The mechanical properties of hydrogels were further explored through compression and tensile tests. The compressive mechanical behavior of hydrogels for use in bone regeneration applications is important because they are primarily subjected to compressive stress. The compressive stress–strain curve obtained through compression testing showed a typical "J-shaped" stress–strain curve at 60% compression for both hydrogel groups, similar to that of biological tissues.[27] Meanwhile, GBM^{gel} exhibited a larger compressive modulus of ≈53.8 kPa (Figure 1L). In the tensile test, GBM^{gel} has a high strain value of 182.8% and tensile stress of 132 kPa, which is significantly superior to the results obtained for GB^{gel} (Figure 1M). This suggests that loading with MBGN enhances the mechanical properties, possibly because of the relatively high surface reactivity, which reduces the physical entanglement of the gelatin and pectin chains in the hydrogel through chemical cross-linking, improving the mechanical properties of the hydrogel matrix. The relative stability of hydrogels in the physiological environment of the body is conducive to their ability to guide cells and avoid deviating from their original position, while also ensuring early support for tissue regeneration. The slow degradation of hydrogels also provides space for the growth of new tissue.[28] Measurement of the swelling and degradation rates of the hydrogels indicated that the swelling rate of GBM^{gel} loaded with MBGN was significantly lower than that of GB^{gel} (Figure 1N), which may be attributed to MBGN cross-linking within the hydrogel, restricting its expansion and contributing to its shape stability. In addition, the degradation rate of GBM^{gel} was noticeably lower than that of GB^{gel}, indicating that the loaded MBGN contributes to the structural stability of the hydrogel (Figure 1O). The detection of Si^{4+} in the loaded MBGN indicates that Si^{4+} is released rapidly during the initial 12 h; however, this was followed by a slower, stable release that was maintained over an extended time period (Figure S3, Supporting Information). This change may be related to the solubility of the ions within the solution. The accelerated release of Si^{4+} in the early stages of hydrogel placement, followed by the sustained slow release after reaching ion equilibrium in the solution, contributes to the immunomodulatory and osteogenic effects of MBGN on the macrophage-stem cell axis, while also reducing the risk of rapid Si^{4+} release, which could lead to toxicity within the body.[29]

2.2. Cell Viability of Hydrogel

The results of the cell viability assays and live/dead staining following the coculture of bone marrow mesenchymal stem cells (BMSCs) with the composite hydrogel for 3 d showed that the BMSCs adhered well to the hydrogel in all groups (**Figure 2**A–C). No significant differences were observed in the cell viability among the various groups as compared to the blank control. These results indicate that the composite hydrogel did not negatively impact the cell viability to any extent. BMSCs were able to attach to and disperse within the hydrogel, suggesting favorable cell-material interaction. The cell counting kit-8 (CCK-8) assay, which measures cell proliferation, further confirmed the biocompatibility of the hydrogel. Cell viability was assessed by coculturing BMSCs with the different hydrogel groups. The results showed no statistically significant differences in terms of the cell survival rate among the various groups as compared to the control group (Figure 2D). The group that was loaded with MBGN showed cell viability similar to that of the group without MBGN, suggesting that MBGN does not adversely affect cell viability. Previous studies have demonstrated the potential toxicity of MBGN in cells. However, amine modification (aMBGN) appears to at least partially mitigate the potential cytotoxicity associated with MBGN, suggesting that modifying the MBGN aided in improving its biocompatibility, rendering it suitable for use in the composite hydrogel. Overall, the results of the in vitro experiments demonstrate that the composite hydrogel, both with and without MBGN loading, is biocompatible and that it supports the viability and growth of BMSCs without any significant cytotoxicity. However, further in vivo studies and long-term assessments are necessary to confirm the safety and effectiveness of the gels in a physiological context.

2.3. In Vitro Experiment

2.3.1. Impact of Hydrogels on Bone Marrow-Derived Macrophages (BMDMs)

Macrophages tend to aggregate around defect sites following the occurrence of a critical bone defect.[30] However, specific pathways that guide macrophages toward the center of the bone defect are often lacking, which often leads to nonunion or delayed healing.[31] One strategy for the targeted repair of critical bone defects involves filling the defect with a hydrogel while simultaneously capturing macrophages. In this study, the polysaccharide BSP, which targets the mannose receptor (MR) on macrophages, was used, as demonstrated previously,[32] and in vitro experiments were performed using primary BMDMs extracted from mice. BMDMs adhere to surfaces when stimulated with a colony-stimulating factor (CSF). Comparison of the effects of CSF and a hydrogel containing BSP on BMDMs indicated that a significant number of BMDMs adhered to the BSP-containing hydrogel, with no significant difference observed as compared to the CSF-stimulated cells (Figure S4, Supporting Information). Additionally, SEM images of BMDMs that were cocultured with the BSP-containing hydrogel showed that the BMDMs were firmly attached to the hydrogel. It is worth noting that the BMDMs exhibited a spherical phenotype after coculturing for 3 d, but

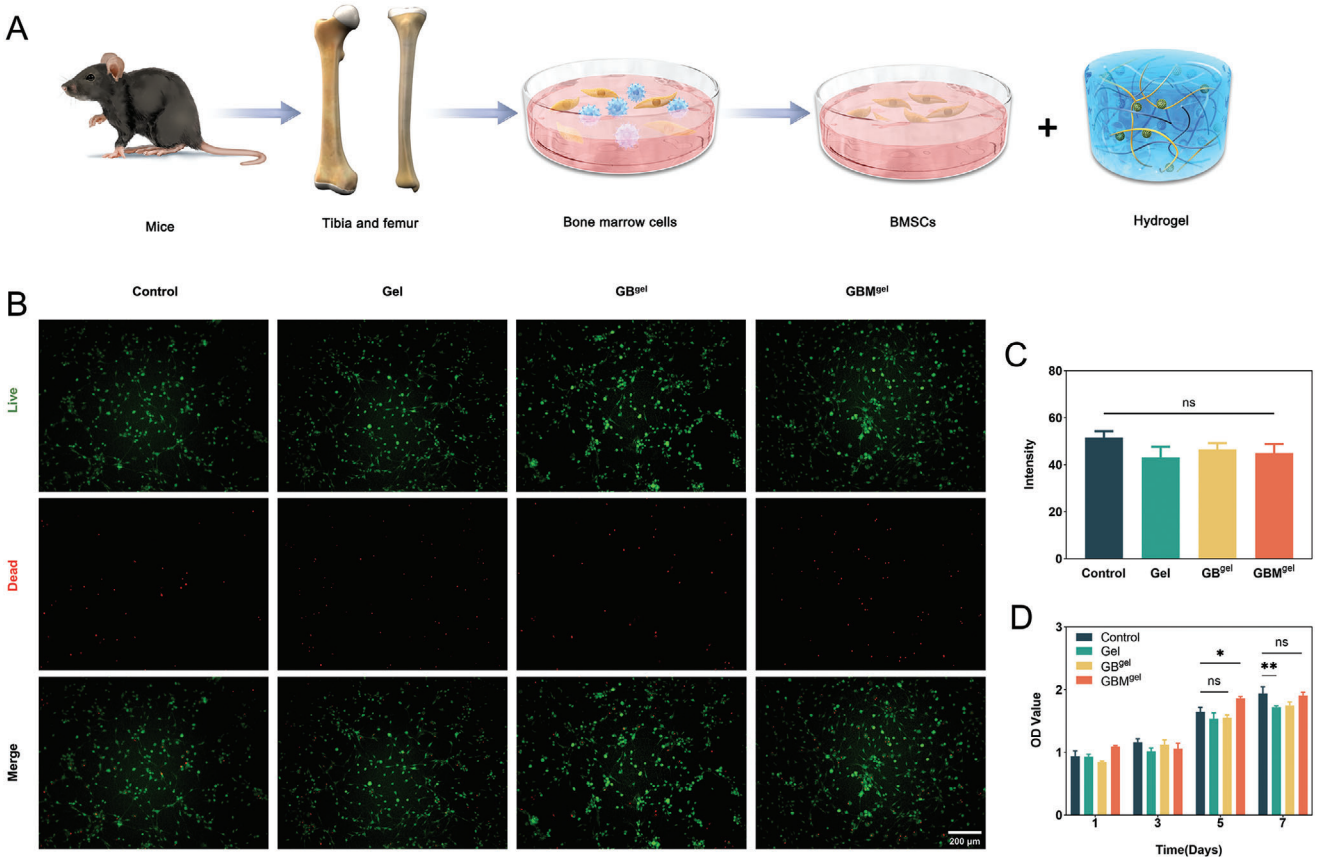

Figure 2. Cell viability. A) Schematic illustration showing the coculture of cells with hydrogel. B) Live/dead staining of BMSCs after 3 d. C) Fluorescence intensity of live BMSCs. D) CCK-8 assay showing BMSC proliferation. (Data presented as mean ± standard deviation, $n = 3$, * for $p < 0.05$, ** for $p < 0.01$. Nonsignificant differences are indicated by "ns.").

transitioned to a more elongated shape with more pseudopodia after 7 d (Figures S5 and S6, Supporting Information), suggesting that capture by the hydrogel may alter the phenotype of the BMDM.[33]

Macrophages, which are crucial participants in the inflammatory response, can polarize to form either the proinflammatory subtype M1 or anti-inflammatory subtype M2 in different immune microenvironments. M1 and M2 macrophages regulate bone regeneration by secreting different cytokines that reshape the immune microenvironment, and their involvement in the inflammatory response is indispensable.[34] The changes that resulted from the hydrogel-targeted of BMDM capture were further explored using flow cytometry, with results showing that after cointervention with lipopolysaccharide (LPS) (100 ng mL^{-1}) to stimulate an inflammatory environment, the proportion of $CD86^+/CD11b^+$ cells was higher and $CD206^+/CD11b^+$ cells lower after 3 d (**Figure** 3A–C), while the proportion of $CD86^+/CD11b^+$ cells showed a decreasing trend and the proportion of $CD206^+/CD11b^+$ cells showed an increasing trend after 7 d (Figure 3D–F). These results reflect the dynamic regulation of BMDM in an inflammatory environment. After 3 d of coculture, both the GB^{gel} and GBM^{gel} groups showed an increased proportion of $CD86^+$ cells as compared to the control and gel groups, whereas no significant increase was observed for the $CD206^+$ cells. M1 macrophages thus preferentially express CD86, whereas M2 macrophages preferentially express CD206. This may be related to the presence of BSP in the hydrogel, because the mannose in the BSP binds to the MR on the BMDMs, influencing polarization toward the M1-type. After 7 d of coculture, the GBM^{gel} group showed the highest proportion of $CD206^+$ cells at 25.9%, which may be related to the presence of MBGN. As time progressed, the MBGN gradually became exposed, and the rich Si^{4+} content in MBGN was confirmed to promote polarization toward M2.

Cell immunofluorescence (IF) staining revealed similar results, with BMDMs stained green to observe the macrophage surface marker F4/80. After 3 d of coculture, the fluorescence of the surface marker inducible nitric oxide synthase (iNOS) on the M1 macrophages showed high intensity in all cell groups (**Figure** 4A), whereas weak fluorescence was observed for the surface marker CD206 in the M2 macrophages. After 3 d of coculture, the GB^{gel} and GBM^{gel} groups showed significantly stronger iNOS fluorescence than the other two groups. However, CD206 fluorescence in the GBM^{gel} group had a higher intensity compared to the other groups on day 7. Additionally, cells within the GBM^{gel} group displayed more elongated morphologies and increased pseudopodia in comparison to the cells within the other groups. Quantitative analysis of the fluorescence corresponding to iNOS and CD206 after 3 and 7 d of coculture revealed similar trends (Figure 4B–E). Based on the phenotypic analysis mentioned above, we conclude

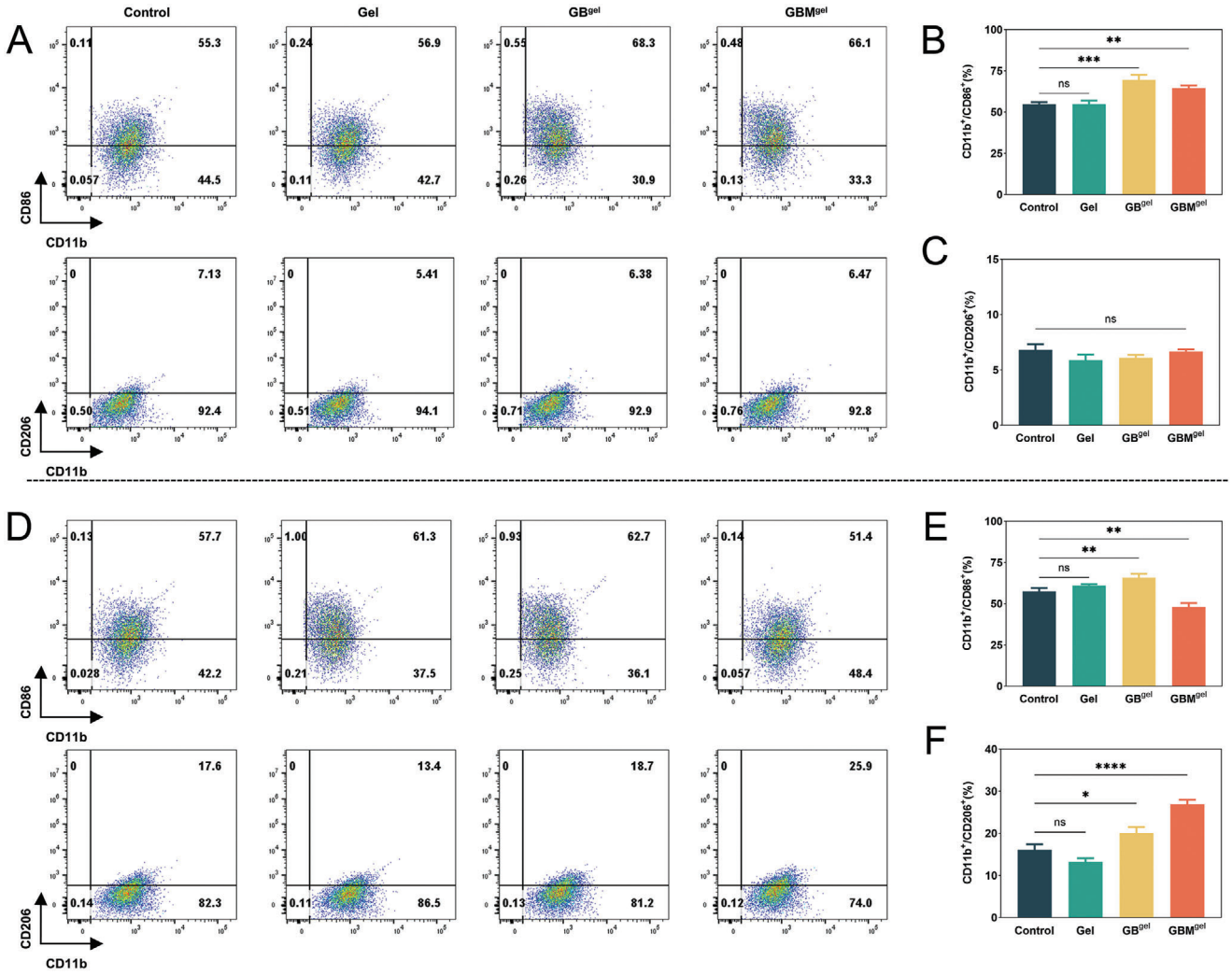

Figure 3. FCA results showing BMDM polarization. A) CD86 and CD206 expression levels resulting from the presence of BMDMs at 3 d, as determined by flow cytometry. B,C) Quantitative analysis of the flow cytometry results on day 3. D) CD86 and CD206 expression levels resulting from the presence of BMDMs at 7 d, as determined by flow cytometry. E,F) Quantitative analysis of the flow cytometry results on day 7. (Data are presented as mean ± standard deviation, $n = 3$, * for $p < 0.05$, ** for $p < 0.01$, *** for $p < 0.001$, and **** for $p < 0.0001$. Nonsignificant differences are indicated by "ns.").

that the coculture of GBM^{gel} with BMDM tended to promote M1 polarization in the BMDMs on day 3, whereas a trend toward M2 polarization was observed on day 7. The GBM^{gel}, which can bind to BMDM receptors early in the process and continuously release Si^{4+} ions, is thus promising for use in ligand-selective targeted capture and the phenotypic transformation of macrophages at different stages.

2.3.2. Impact of Coculturing Hydrogels with BMDM for In Vitro Osteogenesis and Angiogenesis

Following the occurrence of a bone injury, an immune response is immediately initiated, with relevant immune cells accumulating at the defect site and secreting specific cytokines to recruit stem cells. The recruited stem cells then undergo proliferation and differentiation under the regulation of the local microenvironment to facilitate tissue regeneration. In the field of bone immunology, this process represents an endogenous self-healing program. However, in refractory bone defects, inflammatory cells at the damaged site struggle to target the defect, often resulting in prolonged inflammation that hinders stem cell homing, thus impeding tissue regeneration.[35] The homing ability of BMSCs has been shown associating with M1 macrophages.[36] Therefore, cellular scratch assays and transwell chemotaxis migration experiments were conducted to evaluate the effects of BMDMs on the hydrogel targeting of BMSCs, for which BMSCs were cultured within the BMDM-conditioned medium that was obtained after coculturing the BMDMs with hydrogel (Figure S7, Supporting Information). Compared to the group without BSP, both the GB^{gel} and GBM^{gel} groups exhibited higher BMSC migration rates. The migration rate in the GB^{gel} group reached its maximum 30.36% after 24 h, whereas a migration rate of only 10.19% was observed in the control group at this point. The migration rate of the GB^{gel} group peaked after 48 h, reaching at 67.13% (Figure S8A,B, Supporting Information), which is significantly

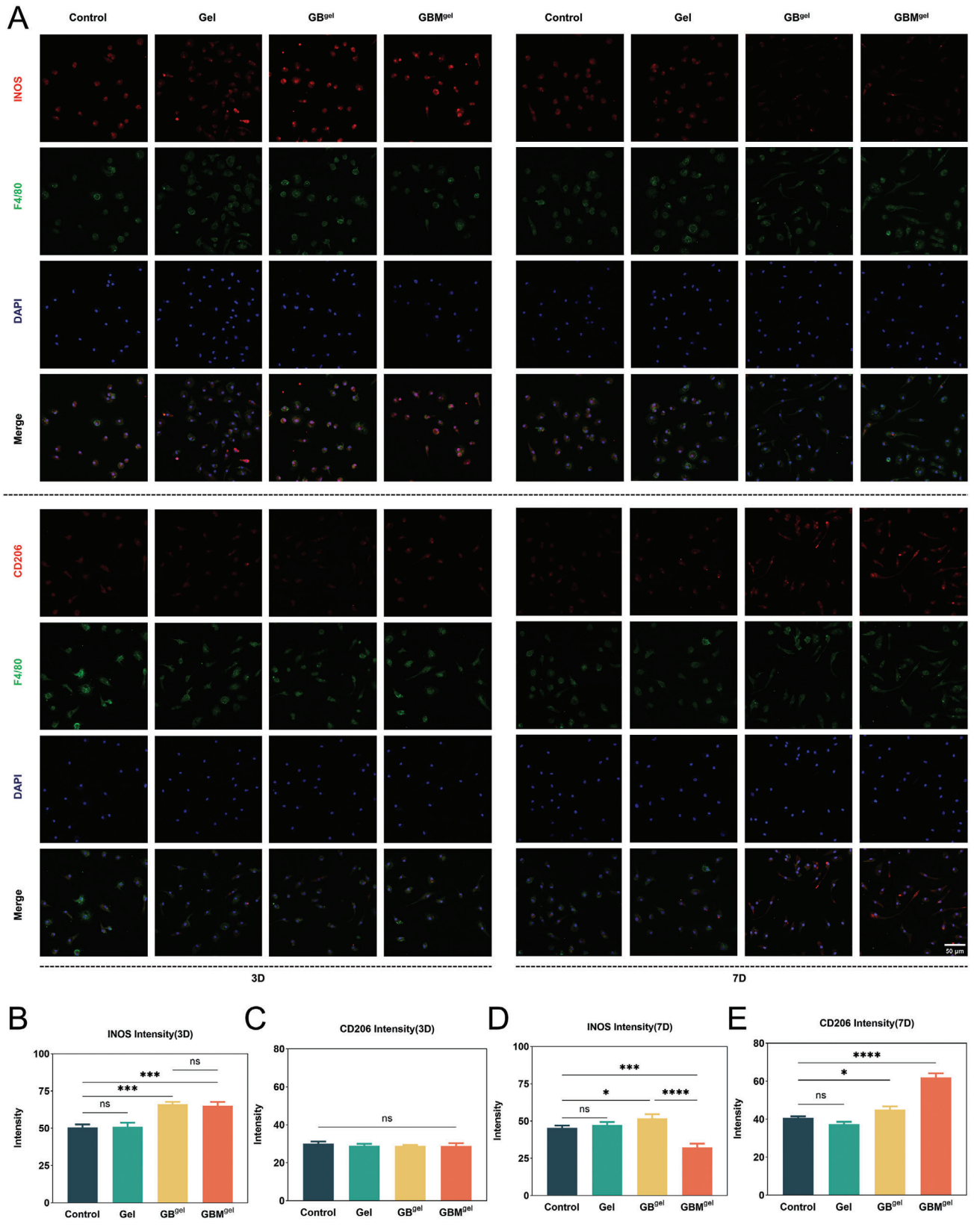

Figure 4. IF analysis of BMDM polarization. A) IF staining showing F4/80, iNOS, and CD206 expression after 3 and 7 d. B) Quantitative analysis of fluorescence intensity for iNOS after 3 and D) 7 d. C) Quantitative analysis of CD206 fluorescence intensity after 3 and E) 7 d. (Data are presented as mean ± standard deviation, $n = 3$, * for $p < 0.05$, *** for $p < 0.001$, and **** for $p < 0.0001$. Nonsignificant differences are indicated by "ns.").

higher than the rate observed in the control and plain gel groups. Transwell migration assays yielded similar results, with BMSCs that were incubated in the culture medium of the GBM^{gel} group, which was cocultured with BMDMs for 7 d, migrated through the transwell membrane after 24 h (Figure S8C,D, Supporting Information). These results suggest that BSP influences the homing ability of stem cells by targeting the BMDMs.

BMDMs secrete the cytokines that are required for BMSC proliferation and osteogenic differentiation.[37] To further explore the influence of the local microenvironment, which is enriched with the osteogenesis-related cytokines that are secreted by BMDMs after hydrogel intervention, cocultures of BMDMs and BMSCs were established upon the osteogenic differentiation of the BMSCs that occurred due to the use of BMDM-conditioned medium. Alkaline phosphatase (ALP), an enzyme that is secreted by osteoblasts, serves as a direct indicator of osteoblast activity and functionality by signifying early osteoblast differentiation and mineralization. BMSCs were harvested for ALP staining and activity assessment after 7 d. The GB^{gel} and GBM^{gel} groups exhibited more prominently stained osteoblasts, with the GBM^{gel} group displaying significantly deeper ALP staining compared to the other groups (**Figure 5**A,B). Osteocalcin (OCN), a calcium-binding protein that is synthesized and secreted by mature osteoblasts, represents a major component of noncollagenous bone protein and is considered a marker of osteoblast differentiation toward mineralization. BMSCs were thus collected for OCN IF staining after 14 d. BMSCs in the GBM^{gel} group exhibited the most intense red fluorescence, indicating the presence of OCN, and displayed superior cell spreading compared to all other groups (Figure 5C). Quantitative analysis of the OCN IF intensity corroborated these findings (Figure 5D). Calcium nodules, which are mineralized ECMs formed by osteoblasts, represent the final stage of osteogenic differentiation. To test for their presence, BMSCs were collected 21 d after coculture and subjected to alizarin red staining, with results showing the most abundant and densely distributed calcium nodules in the GBM^{gel} group (Figure 5E). Quantitative analysis of the calcium nodules yielded results that were consistent with those of the staining (Figure 5F). Quantitative real-time polymerase chain reaction (qRT-PCR)analysis of runt-related transcription factor 2 (RUNX2), ALP, and OCN revealed elevated expression levels in the GBM^{gel} group, aligning with the results of the previous experiments (Figure 5G–I).

Furthermore, the stimulatory effect that coculturing hydrogels with BMDMs has on angiogenesis was assessed through in vitro angiogenesis assays using a specialized culture medium. To test this, the control group was incubated with the specialized culture medium for 4 h, with results suggesting that no significant capillary-like network forms without the presence of the treated macrophages (Figure 5J). In contrast, abundant capillary-like tube formation was observed in the culture media from the GB^{gel} and GBM^{gel} groups, with the GBM^{gel} group exhibiting considerably greater branching and total length (Figure 5K–M). ELISA studies of the cytokines that are related to cell migration and angiogenesis revealed a significant increase in the expression of vascular endothelial growth factor (VEGF) and platelet-derived growth factor-BB (PDGF-BB) in both the GB^{gel} and GBM^{gel} groups, with the GBM^{gel} group showing even greater enhancement than the GB^{gel} group (Figure 5N,O).

2.4. In Vivo Experiments

2.4.1. Establishment of the Animal Model and Hydrogel Implantation

This study focused on investigating the impact of composite hydrogels on the targeting and capturing of macrophages to stimulate the immune cell-related endogenous regenerative program for bone-defect regeneration. Using a rat macrophage-depleted model allowed for effective validation of the impact that the hydrogel has on bone defect regeneration in the absence of macrophages, a method that has previously been proven effective.[38] In this section, a rat cranial defect model is used to investigate the effects of GBM^{gel} on bone defect repair. The injectability and favorable mechanical properties of the GBM^{gel} meant that it could be locally injected and gelled in situ onto a rat cranial defect. Skull specimens were collected 4 and 8 weeks postsurgery to analyze the progress of the repair (**Figure 6**A,B).

2.4.2. Impact of the Hydrogel on Bone Formation and Angiogenesis at the Defect Site

Bone tissue repair was studied using microcomputed tomography (micro-CT) and histological examination. Specimens were collected and subjected to micro-CT scanning before reconstruction to evaluate bone repair. The reconstructed images of the bone defects showed that the normal GBM^{gel} group exhibited significantly better bone repair than the other groups 4- and 8-weeks postsurgery. Four weeks after hydrogel implantation, the normal group that was treated with GBM^{gel} showed new autologous bone tissue formation around the edges of the critically-sized defect, whereas the macrophage-depleted GBM^{gel} group showed little formation. Eight weeks after hydrogel implantation, extensive new bone generation was observed within the critically-sized defect in the normal GBM^{gel} group, with the bone defect almost completely covered by densely-packed new bone tissue (Figure 6C). Some degree of new bone formation was also observed in the macrophage-depleted GBM^{gel} group compared to the macrophage-depleted control group, which may be attributed to the scaffold effect provided by the GBM^{gel}, the cellular microenvironment, and the ability of loaded MBGN to dissolve and promote the formation of a calcium silicate layer upon which bone growth can occur. However, the performance of the macrophage-depleted GBM^{gel} group was inferior to that of the control group. As expected, quantitative micro-CT analysis showed that the normal GBM^{gel} group had significantly higher bone volume/tissue volume (BV/TV) and mineral density (BMD) as compared to the other groups (Figure 6D,E), suggesting that the GBM^{gel} group had a greater number of newly formed and densely packed bone trabeculae. Furthermore, the values of BV/TV and BMD were higher in the normal control group than in the macrophage-depleted GBM^{gel} group, which, in turn, were higher than those in the macrophage-depleted control group. The results of micro-CT and quantitative analysis indicated that GBM^{gel} has a significantly better bone-defect regeneration capacity when macrophages are involved, suggesting that the GBM^{gel} promotes in vivo bone-immune cell endogenous regenerative programs that aid in bone regeneration. Additionally,

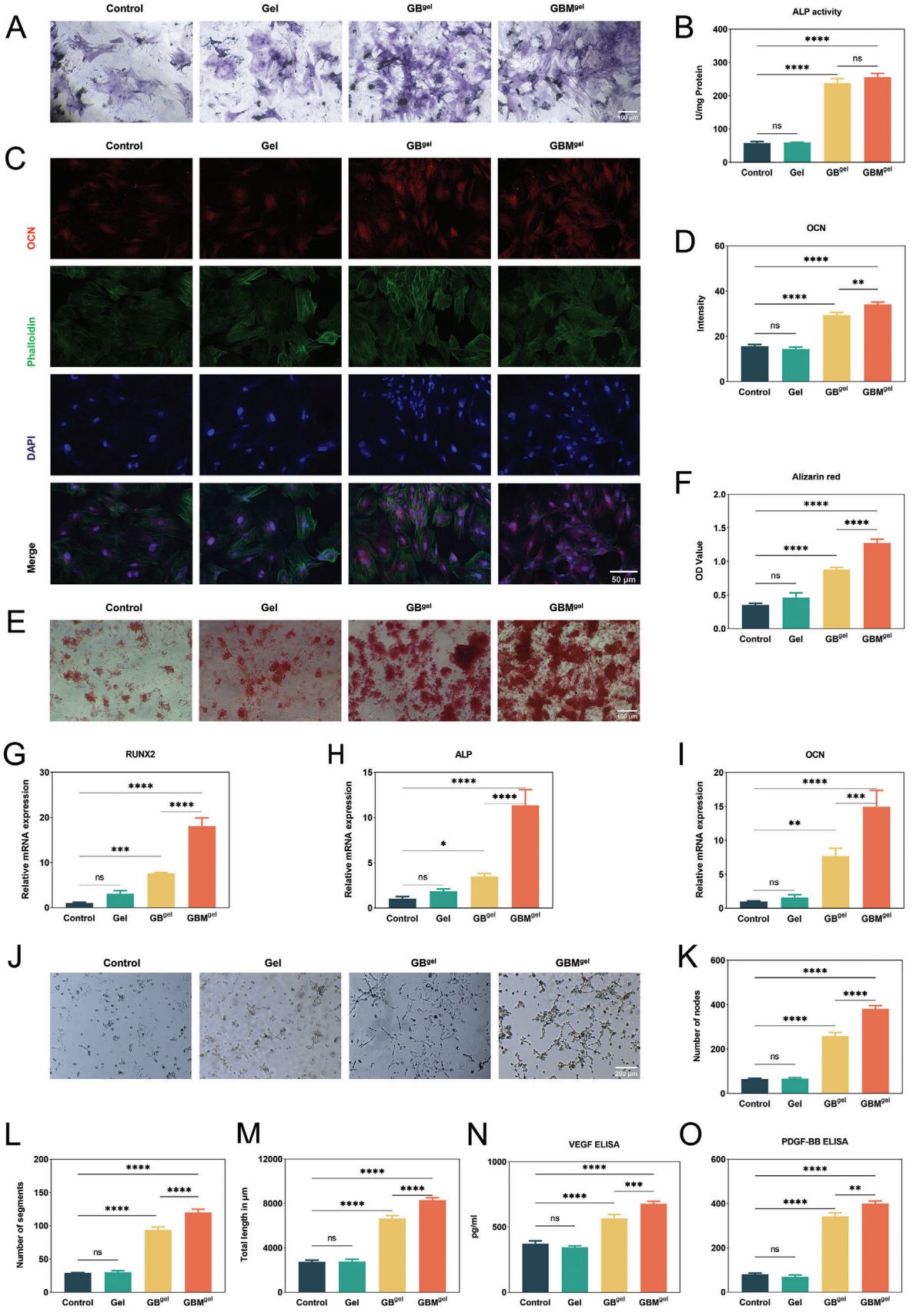

of the macrophage-depleted groups, the GBM^{gel} group exhibited a certain degree of bone regeneration as compared to the control group. However, the bone regeneration was less effective than that of the normal control group, underscoring the importance of macrophages in bone-immune cell endogenous regenerative programs and further highlighting the positive role of GBM^{gel} in site-specific bone regeneration, primarily through the targeted capture of macrophages.

Histological analysis was also conducted on the cranial specimens, with the hematoxylin and eosin (H&E) staining results demonstrating that bone repair was superior in the normal GBM^{gel} group compared to the other groups at different time points; with the normal GBM^{gel} showing the highest continuity of bone tissue regeneration (Figure 6F–H). Masson's staining was used to assess the maturity of the newly formed bone tissue, particularly that of the newly formed to fully remodeled bone, during repair. Red-blue cross-staining indicated the formation of new bone tissue at the defect sites in all groups. However, larger and more continuous areas of red staining were observed for the normal GBM^{gel} group, which was consistent with the quantitative analysis of the red-stained area and indicates enhanced bone formation and remodeling activities for the group. In contrast, the macrophage-depleted GBM^{gel} group exhibited thicker collagen fibers than the normal control group (Figure 6I–K), suggesting that the absence of macrophages in the repair process may result in an inability to precisely regulate stem cell differentiation, leading to the proliferation of scar tissue.

Immunohistochemical (IH) staining of the osteogenic differentiation markers OCN and osteopontin (OPN) indicated that the positive expression of OCN and OPN was significantly higher at different time points in the normal GBM^{gel} group than in the other groups (**Figure** 7A–F), indicating superior bone repair ability. These results suggest that the normal GBM^{gel} group has a better capacity for bone tissue maturation, and variation in the osteogenic markers at different time points suggest that GBM^{gel} had a positive impact throughout the entire process.

To assess the regeneration of blood vessels at the defect site, CD31 IH and von willebrand factor (VWF) IF staining were used to study the level of angiogenesis following the different treatments at the defect site. The results indicated more CD31-positive stained structures in normal mice than in macrophage-depleted rats at 4 weeks. Wounds that were treated with the GBM^{gel} in normal rats showed a higher number of CD31-positive stained blood vessels than the sham surgery group. Conversely, in macrophage-depleted rats, wounds treated with the GBM^{gel} demonstrated a similar number of CD31-positive stained blood vessels as the control group. At 8 weeks, the CD31-stained area showed a decreasing trend (Figure 7G–I). VWF is an indicator of newly formed blood vessels, and at 8 weeks, the expression of VWF in the GBM^{gel} group was significantly lower than that of the macrophage-depleted GBM^{gel} group (Figure 7J–L). This decrease may be attributed to the fact that fewer nutrients and oxygen are required following repair, and the blood vessels that are formed during regeneration subsequently regress. These results indicate that GBM^{gel} can expedite and enhance bone defect healing, even in the absence of macrophages.

2.4.3. Impact of the Hydrogel on Macrophages at the Defect

We hypothesized that the outstanding performance of the GBM^{gel} group in promoting bone and vascular regeneration in the absence of macrophages was based on its ability to target and intervene with the macrophages. To validate this hypothesis, experiments were conducted using samples collected on days 3, 7, and 14 and weeks 4 and 8 postoperation using a macrophage-depleted cranial defect model.

F4/80 was used to label the macrophages and CD90 to label the stem cells. The results showed that significantly less F4/80$^+$ cells were observed at the defect site in the macrophage-depleted rat groups as compared to the normal rat group, indicating that the injection of clodronate liposomes effectively depleted the macrophages (**Figure** 8A–C). Furthermore, the distribution of the CD90$^+$ cells at defect sites was uneven, with cells clustering at the periphery in the macrophage-depleted rats. The number of F4/80$^+$ cells was higher in the GBM^{gel} groups than the control group on day 3, and the CD90$^+$ cells showed a distribution pattern similar to that of the F4/80$^+$ cells, and a noticeable infiltration of F4/80$^+$ cells toward the defect site occurred on day 7, with CD90$^+$ cells distributed accordingly (Figure 8D–F). However, the CD90$^+$ cells were still distributed at the periphery of the defect site in the macrophage-depleted GBM^{gel} group, with no statistically significant difference observed compared with the macrophage-depleted control group.

These results suggest that the distribution of stem cells is influenced by macrophages and that GBM^{gel} can influence the distribution of macrophages but does not directly affect stem cell distribution. Relevant experiments to classify the macrophages in vivo were then conducted, with M1 macrophages labeled using iNOS and M2 macrophages with arginine 1 (ARG-1). On day 3, the GBM^{gel} group with nondepleted macrophages had significantly more iNOS$^+$ cells than ARG-1$^+$ cells, and the proportion of iNOS$^+$ cells was significantly higher than that of the control group. On day 7, there were significantly more ARG-1$^+$ cells than iNOS$^+$ cells in the GBM^{gel} group with nondepleted macrophages, and the proportion of ARG-1$^+$ cells was significantly higher than that of the control group. These experimental results suggest that GBM^{gel} promotes the proportion of M1-type macrophages on day 3 and subsequently promotes the proportion of M2-type macrophages on day 7, indicating that the GBM^{gel} can chronologically polarize macrophages (Figure S9A–C, Supporting Information).

Figure 5. Assessment of in vitro osteogenic activities of BMSCs and angiogenic abilities of HUVECs. A) Light micrographs showing ALP staining. B) Quantitative measurement of ALP activity. C) Immunofluorescence staining of OCN. D) Quantitative comparison of migrated cells in the different conditioned mediums. E) Light micrographs of alizarin red staining. F) optical density values obtained from calcium nodule staining. G) Expression levels of Runx2, H) ALP, and I) OCN. J) Light micrographs indicating endothelial network formation in HUVECs. K) Quantitative analysis of the number of nodes, L) number of segments, and M) total length. N) Quantification of VEGF, and O) PDGF-BB levels obtained using ELISA. (Data are presented as mean ± standard deviation, $n = 5$, * for $p < 0.05$, ** for $p < 0.01$, *** for $p < 0.001$, and **** for $p < 0.0001$. Nonsignificant differences are indicated by "ns.").

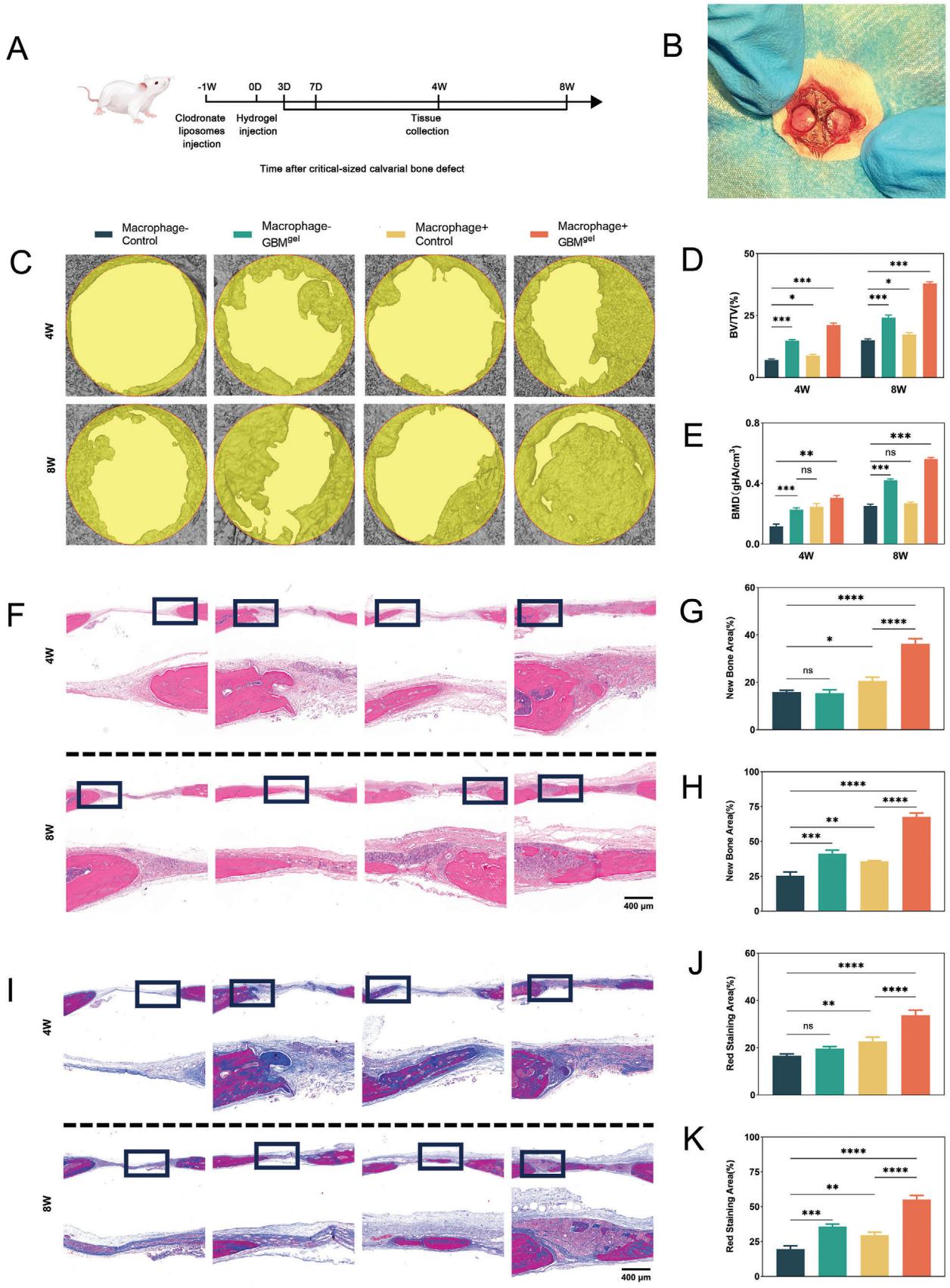

To evaluate the effect of early M1-induced polarization on osteogenesis, RUNX2, an early osteogenic index, was selected for analysis. Groups that were assessed 14 d postsurgery were subjected to IF staining of the RUNX2 areas. The results suggested that the RUNX2$^+$ areas were significantly more abundant in the nonmacrophage-depleted GBM^{gel} group than in the control group, whereas no differences were observed in the RUNX2$^+$ areas of the macrophage-depleted GBM^{gel} group as compared to the control group (Figure 8G,H). This suggests that GBM^{gel} has a bone-promoting effect in the early stages of repair. IF staining of α-smooth muscle actin (α-SMA) at the bone defect site was also performed 8 weeks postsurgery. The aggregation of α-SMA$^+$ cells may indicate pathological encasement by a large number of macrophages.[39] The results suggested no obvious aggregation of the α-SMA$^+$ cells in the GBM^{gel} group with nondepleted macrophages, whereas aggregation was observed in the control group (Figure 8I,J). This may suggest that the macrophage regulation by GBM^{gel} is controllable and that pathological encapsulation can be avoided. PCR analysis of the factors secreted by each group at two different time points indicated that on day 3, the expression of factors such as interleukin (IL)−1, IL-4, IL-12, and tumor necrosis factor-α (TNF-α) was significantly elevated in the GBM^{gel} group with nondepleted macrophages as compared to the control. However, by day 7, their expression showed a significant downward trend, indicating that these factors are highly associated with inflammation. In contrast, the expression of factors such as CSF and oncostatin M (OSM) was significantly higher than it was in the control group on days 3 and 7 (Figure 8K–P). CSF is associated with macrophage recruitment and adhesion, whereas OSM is a key cytokine that directly induces osteogenesis and is a member of the proinflammatory IL-6 family, which is beneficial for bone cell function.[40] This suggests that BSP regulates the characteristics of the macrophages following the occurrence of a bone injury. Similar patterns of cytokine expression have been observed in macrophages treated with different concentrations of BSP and LPS.

2.5. Mechanistic Insights into the Impact of Hydrogels on BMDMs

To further investigate the mechanism by which GBM^{gel} promotes the transition of macrophages to an immunomodulatory phenotype at different time points, a proteomic analysis of cocultured BMDMs was conducted, with mass spectrometry identifying 1877 and 1169 proteins in the control and GBM^{gel} groups, respectively (**Figure 9A**). Several of the proteins showed significant changes (>1.5-fold) in the control and GBM^{gel} groups, with ARG-1, CSF-3, and C-X-C motif chemokine ligand 3 (Cxcl3) upregulated in the GBM^{gel} group (Figure 9B). CSF-3 and Cxcl3 are known to be involved in macrophage recruitment and adhesion, and the observed upregulation suggests that the GBM^{gel} may enhance the recruitment and adhesion of macrophages. ARG-1 contributes to the secretion of anti-inflammatory cytokines by macrophages, and its upregulation suggests that GBM^{gel} may promote the secretion of anti-inflammatory cytokines by macrophages, indicating an immunomodulatory effect. Myeloperoxidase (Mpo) and CD5l expression was downregulated in the GBM^{gel} group. Mpo and cd5l are inflammatory-related factors that are associated with macrophages, and their downregulation in the GBM^{gel} suggests a potential reduction in the inflammatory responses of macrophages in the presence of GBM^{gel}. These proteomic findings provide valuable insights into the molecular mechanisms that underlie the immunomodulatory effects of GBM^{gel} on macrophages at different time points. The upregulation of proteins that are associated with recruitment, adhesion, and anti-inflammatory responses, coupled with the downregulation of inflammation-related proteins, suggests that GBM^{gel} may have implications for tissue regeneration and immunomodulation in biomedical applications. Gene ontology enrichment analysis revealed significant differences in the protein profiles of the GBM^{gel} group as compared to those of the control group, particularly regarding the immune system processes, cell migration, and cell adhesion. These findings suggest that the GBM^{gel} has a pronounced ability to regulate the behavior and polarization of macrophages (Figure 9C). Kyoto encyclopedia of genes and genomes (KEGG) pathway enrichment analysis indicated significant differences between the GBM^{gel} group and the control group in terms of the TNF, nuclear factor kappa-B (NF-κB), phosphatidylinositol 3 kinase/protein kinaseB (PI3K/AKT), and mitogen-activated protein kinase (MAPK) signaling pathways (Figure 9D).

To further validate the impact of the hydrogel on the production of cytokine by the BMDMs, gene expression analysis was conducted using qRT-PCR after 3 and 7 d of coculture. The results showed elevated OSM and CSF expression on 3 and 7 d in the GBM^{gel} group (Figure S10A,B, Supporting Information). The GBM^{gel} demonstrated a sustained ability to promote macrophage and stem cell homing throughout the macrophage intervention. Regarding the expression of inflammatory-related factors iNOS and TNF-α, the GBM^{gel} group exhibited significant upregulation on day 3 but marked downregulation on day 7 (Figure S10C,D, Supporting Information), while no significant difference was observed for the GBM^{gel} and the control groups in terms of the anti-inflammatory factors Arg-1 and IL-10 on day 3. However, Arg-1 and IL-10 were significantly upregulated in the GBM^{gel} group on day 7 (Figure S10E,F, Supporting Information). This may be related to the opposing inflammatory and anti-inflammatory factors at different time points, highlighting the multifaceted beneficial effects of GBM^{gel} in stimulating the early secretion of inflammatory factors by macrophages, mobilizing the osteoprogenitor cells, inducing osteogenic differentiation, and improving vascular formation. Furthermore, after 7 d, as the MBGN within the GBM^{gel} was recognized and internalized by macrophages, a reduction in the expression of inflammatory factors by the

Figure 6. Enhancement of bone regeneration by GBM^{gel} in critical rat bone defects. A) Experimental design. B) Image depicting the critical bone defect model. C) Surface reconstruction of microcomputed tomography for the cranial defect area. D) BV/TV measurement. E) Assessment of BMD in the bone defect area. F) hematoxylin and eosin staining of the critical bone defect at 4 and 8 weeks. G,H) Quantitative analysis of new bone formation at 4 and 8 weeks. I) Masson staining of the critical bone defect at 4 and 8 weeks. J,K) Quantitative analysis of Masson staining (red-stained areas) at 4 and 8 weeks. (Data are presented as mean ± standard deviation, $n = 5$, * for $p < 0.05$, ** for $p < 0.01$, *** for $p < 0.001$, and **** for $p < 0.0001$. Nonsignificant differences are indicated by "ns.").

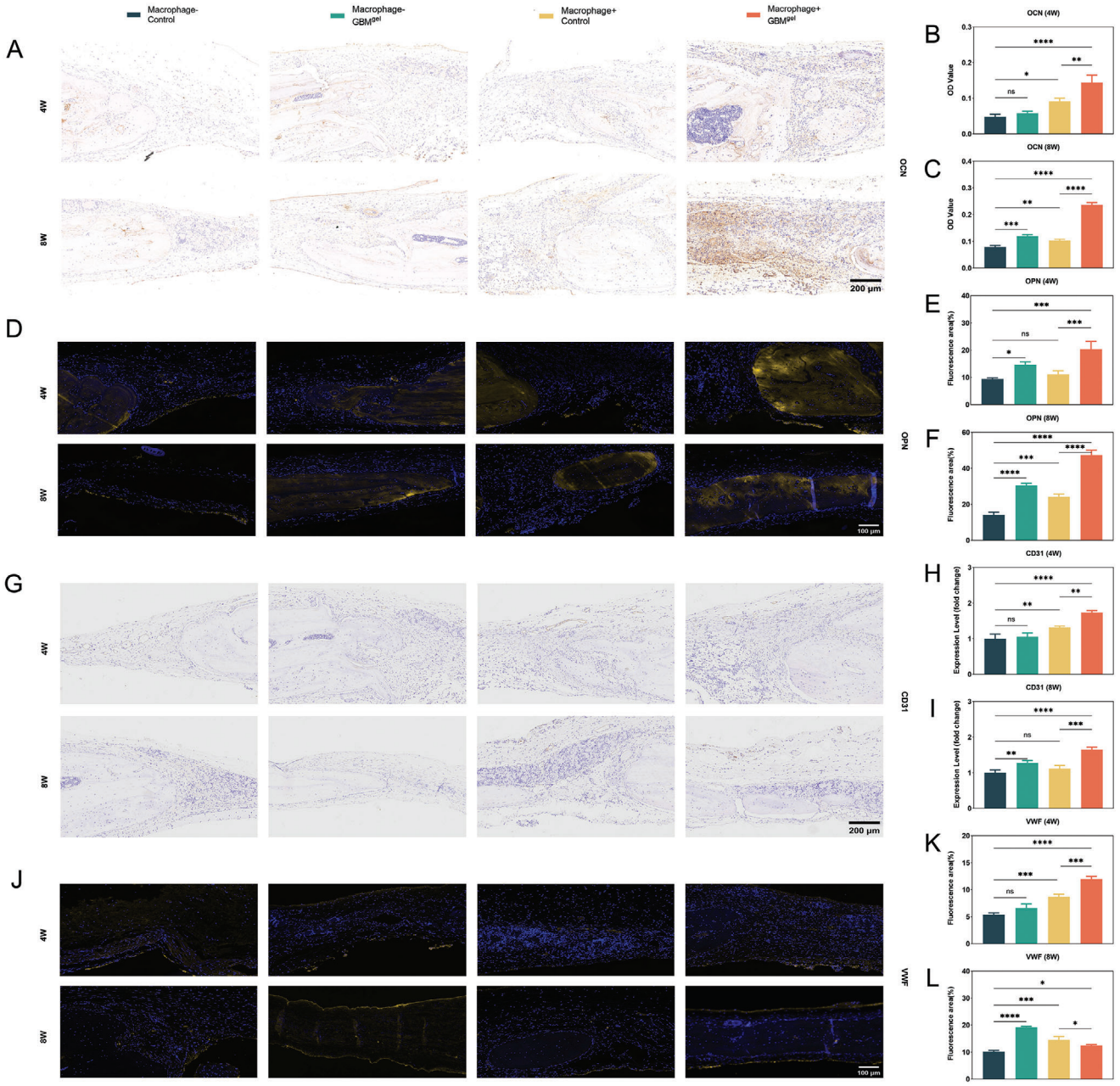

Figure 7. Evaluation of osteogenesis through in vivo histological assessment. A) IH staining of OCN at 4 and 8 weeks. B) Optical density analysis of OCN IH staining at 4 and C) 8 weeks. D) IF staining of OPN at 4 and 8 weeks. E) Quantitative analysis of positively stained areas for OPN at 4 and F) 8 weeks. G) IH staining of CD31 at 4 and 8 weeks. H) Optical density analysis of CD31 IH staining at 4 and I) 8 weeks. J) IF staining of VWF at 4 and 8 weeks. K) Quantitative analysis of positively stained areas for VWF at 4 and L) 8 weeks. (Data presented as mean ± standard deviation, $n = 5$, * for $p < 0.05$, ** for $p < 0.01$, *** for $p < 0.001$, and **** for $p < 0.0001$. Nonsignificant differences are indicated with "ns.").

macrophages was stimulated, prompting the secretion of anti-inflammatory factors to control the inflammation promptly. On day 3, upregulation of CD206 expression was observed in the GBM^{gel} group (Figure S10G, Supporting Information), suggesting that the BSP within the GBM^{gel} may bind to CD206 on the macrophages, indicating a potential mechanism by which the GBM^{gel} can influence the macrophages.

To further understand how the differences between the GBM^{gel} and control groups manifest over time, western blot (WB) experiments were conducted at different time points, focusing on selected pathways that are related to proteomic analysis; namely the JAK/STAT-3, TLR4/NF-κB, and MAPK pathways (Figure 9E). Recent studies have indicated that natural polysaccharides induce immune cell activation through MAPK and NF-κB phosphorylation,[41] and the WB results revealed that the expression of p-NF-κBp65/NF-κBp65 and p-ERK/ERK was increased in the GBM^{gel} group compared to the control group by day 3 (Figure 9F–H). However, no significant differences in the

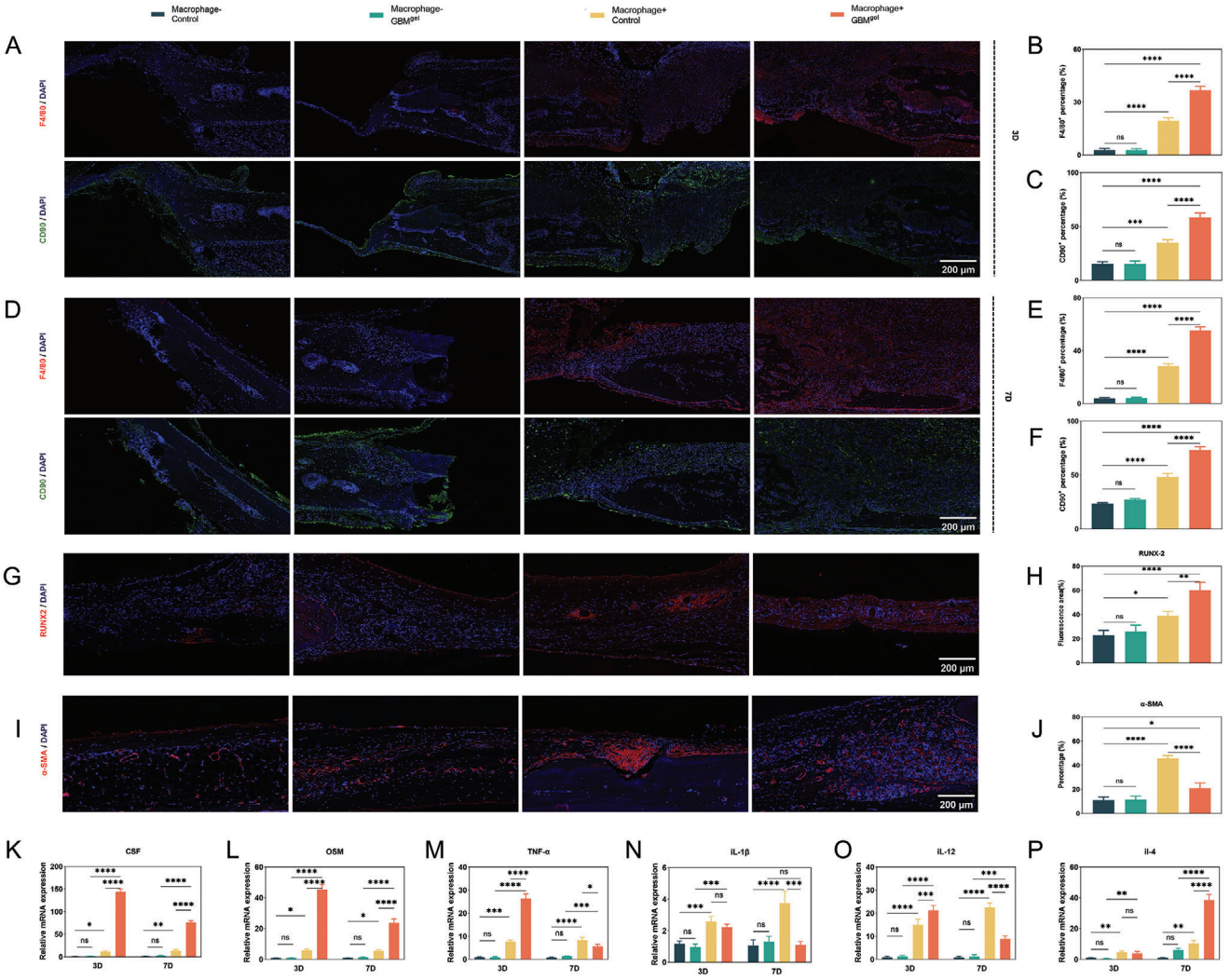

Figure 8. Histological assessment of immunomodulation in vivo. A) IF staining of F4/80 and CD90 after 3 d. B) Percentage of F4/80$^+$ cells on day 3. C) Percentage of CD90$^+$ cells on day 3. D) IF staining of F4/80 and CD90 on day 7. E) Percentage of F4/80$^+$ cells on day 7. F) Percentage of CD90$^+$ cells on day 7. G) IF staining of RUNX2 on day 14. H) Fluorescence area of RUNX2 on day 14. I) IF staining of α-SMA after 8 weeks. J) Percentage of α-SMA$^+$ cells after 8 weeks. K) Expression of osteogenesis-related genes in CSF, L) OSM, M) TNF-α, N) IL-1β, O) IL-12, and P) IL-4. (Data presented as mean $\pm$ standard deviations, $n = 5$, * for $p < 0.05$, ** for $p < 0.01$, *** for $p < 0.001$, and **** for $p < 0.0001$. Nonsignificant differences are indicated by "ns.").

expression of p-NF-κBp65/NF-κBp65 or p-ERK/ERK were observed compared to the control group on day 7, and significant upregulation was observed in the expression of p-STAT3/STAT3 (Figure 9I). These results suggest that in the early stages, the GBM^{gel} group activates the NF-κB signaling pathway by binding to the TLR4 receptor, promoting the BMDMs to polarize toward the M1 phenotype while simultaneously activating the ERK signaling pathway to limit the release of inflammatory factors. The significant upregulation of the JAK/STAT3 signaling pathway in the later stages promotes BMDMs to polarize toward the M2 phenotype. These results further indicate that the GBM^{gel}, compared to the GB^{gel} without MBGN, exhibits significant enhancement in precisely regulating polarization and the release of related cytokines.

In summary, these results imply that the medium that has been conditioned with macrophages containing BSP initiates the healing process through chemotactic effects, whereas the presence of loaded MBGN promotes stem cell differentiation in a specific direction. These findings further underscore the precise immunomodulatory properties of the GBM^{gel}, which are beneficial for both vascular formation and osteogenesis.

3. Conclusion

In summary, the results of this study demonstrate that the application of biomaterial ligands for the selective targeting and capture of macrophages, coupled with the promotion of M1 polarization in the early stages and M2 polarization in the later stages, contributes to the activation of the bone immune-stem cell-based intrinsic self-healing program. Additionally, a composite hydrogel that was composed mainly of BSP and gelatin that incorporates MBGN was developed for experimentation. By exploring

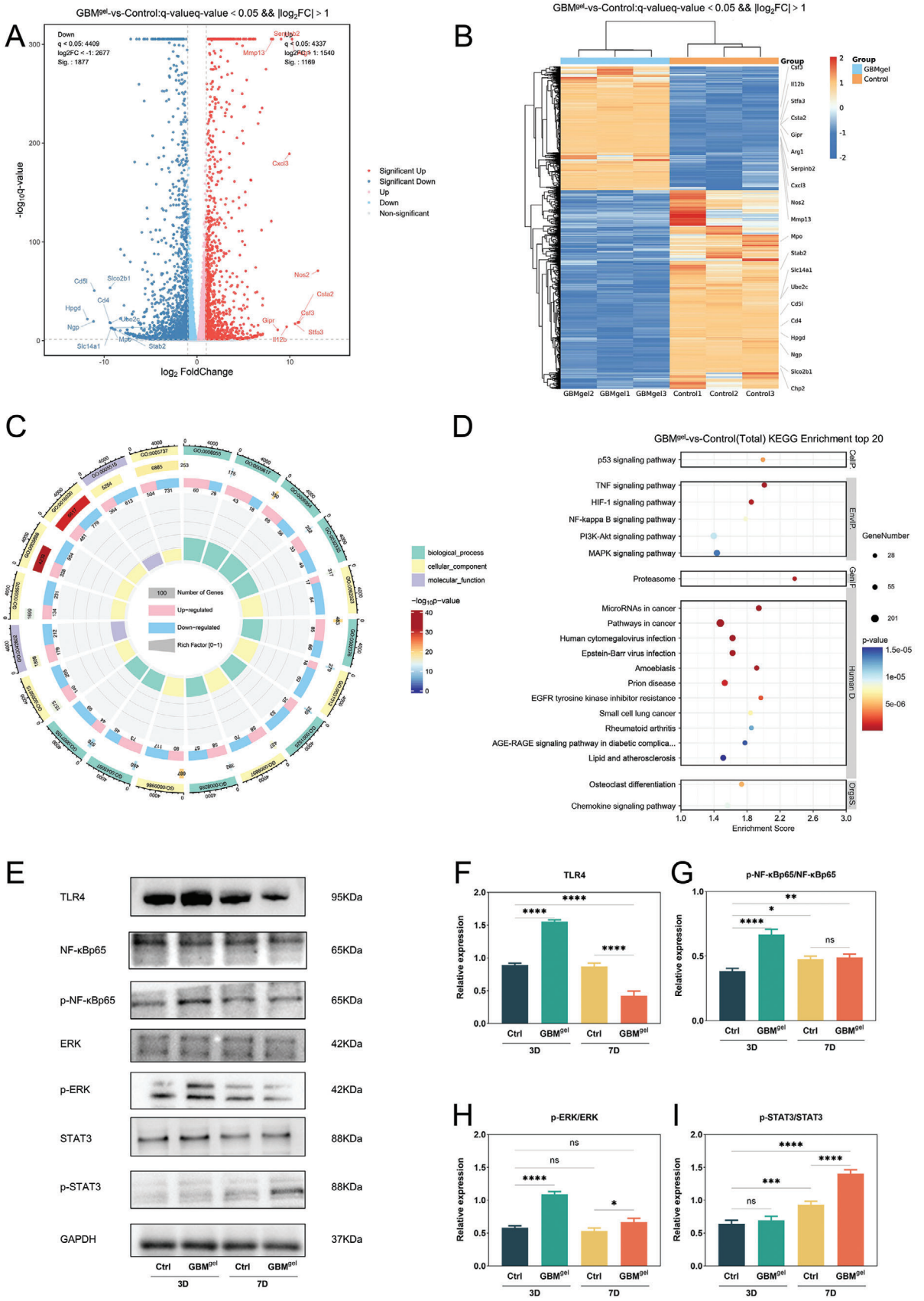

the relevant mechanisms, the role of macrophages in the intrinsic self-healing of bone immune-stem cells was elucidated, confirming that the targeted capture of macrophages is an effective means of promoting bone defect regeneration.

4. Experimental Section

Preparation of oBSP: BSP powder derived from the root of *B. striata* (Panier Biotech, Xi'an, China) (4 g) was subjected to ultraviolet sterilization and then dissolved in deionized water to prepare a 2% w/v solution. Sodium NaIO4 (50 mL) was added as an oxidizing agent (Aladdin, Shanghai, China) and the reaction was stirred under protection by argon in the dark for 8 h. Ethylene glycol (Aladdin) was added to terminate the reaction, the resulting product was transferred to a dialysis bag with a molecular weight cutoff of 3500 and dialyzed in deionized water for 48 h. After dialysis, the solution was filtered, stored at −20 °C, and freeze-dried for 48 h to obtain oBSP. The degree of oxidation in the oBSP was determined using a previously reported method, in which oBSP was reacted with excessive amounts of tert-butyl carbazate (t-BC, TCI, Shanghai, China), and unreacted t-BC was quantified by adding 2,4,6-trinitrobenzenesulfonic acid (TNBS, Sigma-Aldrich, USA). The degree of oxidation was determined by measuring the colored derivatives produced by the excess t-BC and TNBS reactions at 334 nm using a spectrophotometer, with results showing 70.5% oxidation.

Preparation of aMBGN: MBGN was synthesized following procedures previously mentioned. A buffer solution of Tris hydrochloride (Macklin, Shanghai, China) (500 mL) was prepared at pH 8, and a specified amount was placed in a flask and stirred at 60 °C. Cetyltrimethylammonium bromide (Sigma-Aldrich) (1.5 g), calcium nitrate tetrahydrate (Macklin) (2.45 g), tetraethyl orthosilicate (Macklin) (11.5 mL), and triethyl phosphate (Macklin) (0.9 mL) were then added to the flask and the reaction allowed to proceed for 24 h before termination by 5000 g centrifugation. The resulting product was washed three times with anhydrous ethanol and deionized water, dried, and finally calcined at 650 °C for 3 h to obtain MBGN. MBGN (0.4 g) was then placed in n-hexane, agitated, and APTES (Sigma-Aldrich) (5 mL) was added. The mixture was then stirred at 60 °C for 24 h, and the product washed three times in anhydrous ethanol and deionized water before drying to obtain aMBGN.

Preparation of GB^{gel} and GBM^{gel}: Gelatin and oBSP (Aladdin) were dissolved in PBS at a concentration of 20% and stirred until uniform. The two liquids were then mixed at room temperature so that the excess amino groups on the gelatin could react with the aldehyde groups on the oBSP, resulting in the formation of the GB^{gel} hydrogel. oBSP was then dissolved in PBS at a concentration of 20%, stirred until uniform, and aMBGN dissolved in the oBSP solution at a concentration of 6%. The mixture was then stirred using a magnetic stirrer until well mixed at room temperature so that the aldehyde groups on the oBSP and amino groups on the aMBGN could undergo a Schiff base reaction and form covalent bonds. The mixture was then mixed with an equal concentration of gelatin solution, allowing the excess hydroxyl groups on the MBGN to form hydrogen bonds with the carboxyl groups on the gelatin, resulting in the formation of the GBM^{gel}.

SEM and TEM: The surface morphologies of MBGN, aMBGN, GB^{gel}, and GBM^{gel} were observed using SEM (Hitachi, S-4800, Japan) and TEM (FEI, F20, USA). Prior to testing, MBGN and aMBGN were dispersed in anhydrous ethanol and drop-cast onto silicon wafers, followed by air drying. The samples were then affixed to specimen mounts using a sputter coater (Quorum Technologies, SC7620, UK) and gold coated over 60 s to enhance conductivity. The hydrogel samples were then freeze-dried for 3 d and rendered brittle by freezing in liquid nitrogen before testing. EDS elemental analysis was also conducted to determine the presence of C, O, Si, Ca, and N on the sample surfaces.

Particle Size Analysis: For particle size analysis, MBGN and aMBGN were dispersed in anhydrous ethanol via ultrasonic dispersion, and analysis performed using a research-grade light scattering system (Malvern, UK).

XRD: The synthesized MBGN was analyzed using XRD (Ultima III, Japan) over a diffraction angle range of 10–80° (2θ) at a scanning speed of 2° min^{-1}, using Cu Kα radiation with a tube current and voltage of 40 mA and 40 kV.

FT-IR Analysis: FT-IR (Thermo Scientific, USA) was used to acquire FT-IR spectra for dried MBGN, aMBGN, BSP, oBSP, GB^{gel}, and GBM^{gel} samples across the range 4000–500 cm^{-1}.

Observation of Hydrogel Cross-Linking: The gelation of cross-linked hydrogels was determined using the small bottle tilt method. Briefly, 2 mL of gel was added to a glass bottle at 37 °C at different time periods to determine the time at which the gel solution no longer flowed after tilting the small bottle. This method allows the gelation process to be effectively observed. Photos were taken before and after the hydrogel cross-linking.

Rheological Behavior: The rheological properties of the hydrogel samples were assessed using a rheometer (Thermo Scientific, HAAKE RheoStress 6000). For testing, hydrogel samples ($d = 25$ mm, $h = 2$ mm) were placed on the sample stage and frequency and strain tests conducted at 37 °C using a flat plate device with a diameter of 25 mm. The storage and loss moduli of the hydrogels were then measured under an oscillation frequency varying from 0.1 to 12.5 Hz with the shear strain value fixed at 5%. The storage and loss moduli were also measured under shear strain ranging over 1–1000% with the oscillation frequency fixed at 1 Hz.

Hydrogel Injectability: The injectability of the GBM^{gel} was evaluated through macroscopic observation and rheological measurement, for which GBM^{gel} was drawn up using a 1 mL medical syringe, cross-linked, and injected into a PBS solution for direct observation of its injectability. The shear viscosity of the GBM^{gel} was measured by steady-state rheological scanning. Tests were conducted at room temperature, with a test gap of 1 mm, a strain of 1%, and a shear rate range of 1–100 s^{-1}.

Hydrogel Self-Healing Activity: The self-healing activity of the GBM^{gel} was evaluated through macroscopic observation and rheological measurement. To test the self-healing ability, two pieces of GBM^{gel} were dyed different colors, placed in a mold, and cut. The two cut hydrogels were then placed together at 37 °C for 30 min, and the self-healing performance macroscopically analyzed by direct observation of the reconstructed hydrogel. Cylindrical GBM^{gel} ($d = 25$ mm, $h = 2$ mm) was also placed on a rheometer and self-healing evaluated by alternate strain scanning at 1% and 1000%, with a strain interval of 1 min. A total of four cycles were performed. Tests were conducted at room temperature, with the oscillation frequency fixed at 1 Hz.

Mechanical Properties: To evaluate the mechanical properties of the hydrogels, samples were examined using a universal mechanical tester (Hengyi, HY-1080, Shanghai, China). Hydrogels were molded into different shapes for compression and tensile tests. A cylinder ($d = 10$ mm, $h = 5$ mm) prepared as a compression sample was then subjected to compression at a rate of 5 mm min^{-1}, and the compression modulus of the hydrogel was determined by calculating the slope of the stress–strain curve that passed through the origin. Compression was ceased at 60%. Tensile testing was performed using a sample with a width of 25 mm, thickness of 2.5 mm, and length of 5 mm, which was subjected to tensile force that was increased at 20 mm min^{-1}. The test was considered complete when the hydrogel broke.

Figure 9. Transcriptome sequencing and western blot experiments investigating the mechanism by which GBM^{gel} regulates macrophage polarization. A) Volcano map showing differentially expressed genes (DEGs) in the GBM^{gel} group as compared to the control group. B) Heat map of DEGs. C) Gene ontology enrichment analysis of DEGs. D) KEGG enrichment analysis of DEGs. E) Representative western blot images F) Quantitative analysis of toll-like receptor 4 (TLR4) expression, G) NF-κBp65 phosphorylation levels of, H) extracellular signal-regulated Kinases (ERK), and I) signal transducer and activator of transcription 3 (STAT3). (Data presented as mean ± standard deviation, $n = 3$, * for $p < 0.05$, ** for $p < 0.01$, *** for $p < 0.001$, and **** for $p < 0.0001$. Nonsignificant differences are indicated by "ns.").

Hydrogel Swelling and Degradation Rates: The swelling ratio of the hydrogels in PBS was assessed at pH 7.4 to evaluate in vitro swelling. In brief, ≈1 mL of freshly prepared hydrogel was added to 3 mL of PBS at 37 °C and removed periodically for measurement of the mass. The swelling ratio was calculated using Equation (1)

$$\text{Swelling Ratio}\ (\%) = \frac{W_1 - W_0}{W_0} \times 100\% \quad (1)$$

where W_1 is the mass of the hydrogel after immersion in PBS and W_0 is the mass of the hydrogel before immersion in PBS.

Similarly, the degradation rate of the hydrogels in PBS with a pH of 7.4 was evaluated to assess in vitro degradation. In brief, ≈1 mL of freshly prepared hydrogel was added to 3 mL of PBS at 37 °C. The PBS was then removed periodically, and the mass of the hydrogel measured. The degradation rate was calculated using Equation (2)

$$\text{Degradation Rate}\ (\%) = \frac{W_0 - W_2}{W_0} \times 100\% \quad (2)$$

where W_2 is the mass of the hydrogel after immersion in PBS and W_0 is the mass of the hydrogel before immersion in PBS.

Silicon Ion Release Experiment: An equal volume of the material was introduced into 1 mL of simulated body fluid, replaced at specific intervals, and the resulting supernatant gathered. The silicon ion concentration in the supernatant collected at each time point was determined using inductively coupled plasma emission spectroscopy (Optima 7300, PerkinElmer, USA).

Cell Viability Assay: Following a protocol approved by the Ethics Committee of Soochow University (Approval No. SUDA20231211A05), BMSCs were obtained from 8-week-old male C57 mice and employed for in vitro experiments. BMSCs were cultured in alpha minimal essential medium (α-MEM, Gibco, USA) supplemented with 10% fetal bovine serum (FBS, Gibco) and 1% penicillin/streptomycin (P/S, Gibco). The culture was then maintained at 37 °C in a 5% CO_2 incubator and BMSCs were seeded onto sterile hydrogel discs ($d = 8$ mm, $h = 1$ mm, sterilized with 75% ethanol) in 48-well plates at a density of 1×10^4 cells per well. Cell proliferation on the hydrogel was assessed using the CCK-8 assay on days 1, 3, 5, and 7, following the manufacturer's instructions. The optical density (OD) value at 450 nm was measured at specified intervals using a microplate reader ($n = 3$). After 3 d of culture, the cell viability on the hydrogel was evaluated using a calcein acetoxymethyl ester/propidium iodide live/dead staining kit and examined with laser confocal microscope. Quantitative measurement of cell viability was conducted using ImageJ software (National Institutes of Health, Bethesda, USA).

Cell Culture and Conditioned Medium Collection Translation: In accordance with the protocol approved by the Ethics Committee of Soochow University, BMSCs and primary mouse BMDMs were isolated from 8-week-old male C57 mice. BMDMs were obtained from mouse bone marrow and cultured for 6 d at a concentration of 1×10^6 cells mL^{-1} in culture medium CSF at a concentration of 20 ng mL^{-1}. BMSCs from passages 3–5, also derived from mouse bone marrow, were used for the experiments. BMDMs were seeded at a density of 3×10^6 cells per well in a six-well plate and cultured in dulbecco's modified eagle medium (DMEM) supplemented with FBS and P/S. The culture medium was collected after 48 h and subjected to centrifugation at 1000 rpm for 3 min, and the resulting supernatant was collected, stored, and labeled as the control culture medium. Simultaneously, sterile hydrogels were placed at the bottom of a six-well plate, and BMDMs were seeded at a density of 3×10^6 cells per well in six-well plates containing the hydrogel. The cells were then cocultured for a specific period in DMEM supplemented with FBS and P/S. The culture medium was then collected, centrifuged at 1000 rpm for 3 min, and the supernatant collected, stored, and labeled.

Morphological and Behavioral Analysis of Cocultured Macrophages: Macrophages that were cocultured with hydrogel for a specific duration were subjected to fixation with 4% paraformaldehyde at room temperature for 30 min before samples were prepared using the alcohol gradient dehydration method and subsequently coated with gold over 60 s using a sputter coater to allow observation of the macrophages with SEM and TEM.

Polarization Analysis: Flow cytometric analysis was conducted using a flow cytometer (BD, Canto II, USA) to assess the expression of the macrophage markers CD86, CD206, CD11b, and CD45 in the cocultured BMSCs. Cells were subjected to two cold PBS washes and then stained with fluorescein isothiocyanate-conjugated anti-CD86 (BD Pharmingen, USA), phycoerythrin-conjugated anti-CD206 (BD Pharmingen), allophycocyanin-conjugated anti-CD11b (BD Pharmingen), and phycoerythrin-cyanine7-conjugated anti-CD45 antibodies (BD Pharmingen). Staining was employed to assess the macrophage polarization. IF analysis of the macrophage markers iNOS (Abcam, UK), CD206 (Abcam), and F4/80 (Abcam) in the cocultured BMSCs was performed using a laser scanning confocal microscope (ZEISS, LSM800, Germany). Cells were fixed using 4% paraformaldehyde (Biosharp, Shanghai, China), blocked with a rapid blocking solution, and subsequently incubated with primary and secondary antibodies, and 4′,6-diamidino-2-phenylindole (DAPI, Yeasen, Shanghai, China). IF-labeled cells were then observed under a microscope and images captured for analysis.

BMSC Migration Assay: BMSCs were seeded in six-well plates (Corning, USA) at a density of 1×10^6 cells per well and cultured for 24 h. The culture medium was then aspirated and a scratch created at the bottom of each well using a 200 µL pipette tip. Subsequently, the cells were rinsed twice with PBS, and various BMDMs-conditioned media added to continue the culture. Cells were periodically observed using an inverted microscope (DMI 3000 B, Leica, Germany), and images were captured at different time points to monitor the migration of cells into the scratched area. For the transwell migration assay, BMSCs were seeded in the upper chamber of a 24-well transwell plate (Corning) at a density of 2×10^5 cells per well and cultured in fresh DMEM without FBS and P/S. Different BMDM-conditioned culture media were also added to the lower chamber of the 24-well transwell plate and incubated for 12 h. Following incubation, the upper chamber was removed from the plate and the cells fixed with 4% paraformaldehyde (Biosharp) before staining with crystal violet. Cell observation and image capture were performed using an inverted microscope.

Osteogenic Differentiation: BMSCs were seeded in 24-well plates at a density of 5×10^4 cells per well and allowed to incubate overnight before exposure to various prepared BMDM-conditioned culture media. The culture medium was refreshed every other day. Following a 7-d culture period, the various BMSC groups were subjected to staining and ALP activity quantification, which was conducted using an ALP staining kit (Beyotime, Shanghai, China) and an ALP activity quantification kit (Jiancheng, Nanjing, China). After a 14-d culture period, immunofluorescent staining of the different BMSC groups was performed using an OCN primary antibody (SAB, USA), following a previously described IF staining procedure. Upon coculturing for 21 d, the BMSCs were stained to observe calcium nodules using an alizarin red calcium staining kit (Cyagen, Guangzhou, China). Calcium nodules were subsequently observed and photographed using optical microscopy. The calcium nodules were then dissolved in hydrochloric acid, and their absorbance measured at 420 nm using a microplate reader. Total RNA was extracted from the osteogenic cells at various time points for qRT-PCR. BMSCs were cocultured for a duration of 7 and 14 d before total RNA was extracted using Trizol reagent. The extracted RNA was then subjected to reverse transcription to obtain complementary DNA (cDNA) using a reverse transcription kit from Takara (Shiga, Japan). The MaximaTM SYBR Green/ROX qPCR Master Mix from Thermo Fisher Scientific was employed for qRT-PCR analysis. All reactions were conducted in triplicate with β-actin as the internal reference gene. The primer sequences were designed by PubMed and synthesized by Shanghai Generay (Table S1, Supporting Information).

Angiogenesis Experiment with HUVECs: HUVECs were cultured in 24-well plates (Corning), coated with a low-growth factor matrix gel at a density of 1×10^5 cells mL^{-1}, and maintained in a culture medium specific for BMDMs. After a 3 d incubation period, cells were fixed using 4% paraformaldehyde, examined under an inverted fluorescence microscope, and images were captured. Quantitative analysis was performed using ImageJ software. In addition, cell culture supernatants were collected and

the VEGF and PDGF-BB levels quantified using ELISA kits (Elabscience, Wuhan, China) in accordance with the manufacturer's instructions.

Preparation of Experimental Animals: Sprague–Dawley (SD) rats from Zhaoyan New Drug Research Center Co., Ltd. (Suzhou, China) were employed for animal experiments. Rats were exclusively male and weighed ≈200–220 g on average. All animal-related procedures and surgeries were carried out in strict adherence with the ethical guidelines approved by the Ethics Committee of Soochow University (Approval No. SUDA20231211A05).

Establishment of Rat Models and Hydrogel Implantation: To establish a rat model with depleted macrophages, clodronate liposomes (Yeasen) were intraperitoneally administered 1 week before the surgical procedure and continued once weekly postsurgery to deplete macrophages in the SD rats. The surgical procedure commenced after 1 week of chloroquine treatment. Rats were then anesthetized with 2% pentobarbital (2.5 mL kg^{-1}), their heads shaved and their skin disinfected with an anionic solution before a longitudinal incision, ≈2.5 cm in length, was made along the midline of the skull. Subsequently, the skin and fascia layers were meticulously separated until the skull was exposed. Two circular defects, each with a diameter of 5 mm, were created on both sides of the skull using a trephine drill. After rinsing to control bleeding, a nongelled hydrogel was injected in situ to cover the wound and allowed to gel for 10 min. The control group received an equal volume of PBS by injection. The incision was meticulously sutured layer-by-layer and disinfected with iodine. Starting from the day of surgery, penicillin was administered via intramuscular injection for three consecutive days as a preventive measure against infection.

Collection of Animal Specimens: SD rats were humanely euthanized 3 d, 7 d, 14 d, 4 weeks, and 8 weeks after surgery. Skull specimens were then carefully retrieved from the respective groups and fixed in 4% paraformaldehyde (Biosharp) for a duration of 24 h.

Micro-CT Analysis: Micro-CT scanning and processing of the skull samples 4 and 8 weeks postsurgery were performed using a Micro-CT system (SkyScan 1176, Belgium). The scanning parameters were set with a scanning voltage of 65 kV, a current of 385 mA, and a resolution of 7 µm. The radial, sagittal, and coronal cross-sections of the radius were reconstructed with the assistance of CTAnalyzer software (Skyscan). Circular regions of interest were defined for the purpose of morphological and histological analyses, including the assessment of BV/TV at the fracture site and BMD. The resultant sample models generated by the software were further subjected to surface reconstruction through the use of Mimic software (Belgium).

Histological Analysis: Skull samples were decalcified in an ethylenediaminetetraacetic acid (Biosharp) solution for 4 weeks, then dehydrated using a sequence of ethanol solutions with different concentrations. Samples were then immersed in pure xylene and embedded in paraffin wax. Histological analysis consisted of two distinct components. Samples from postoperative days 3 and 7 were processed as described above; decalcified, embedded, sectioned, and subjected to IF staining with antibodies against F4/80 (Abcam), CD90 (Abcam), iNOS (Abcam), and ARG-1 (Abcam) to examine the distribution of macrophages and stem cells within the tissue. Samples collected on postoperative day 14 were subjected to IF staining with an antibody against RUNX2 (Abcam). Samples from weeks 4 and 8 postsurgery were analyzed using H&E staining and Masson's trichrome staining to evaluate bone regeneration. IH staining was performed for OCN (Abcam) and CD31 (Abcam), and IF staining for OPN (Abcam) and VWF (Abcam). These markers were used to assess bone tissue vascularization, periosteum regeneration, and bone defect healing.

qRT-PCR In Vivo: Samples collected on postoperative days 3 and 7 were immediately frozen in liquid nitrogen and subsequently ground. Total RNA extraction was performed on each sample using TRIzol reagent (Invitrogen, USA). The extracted RNA was then reverse-transcribed into cDNA using a reverse transcription kit from Takara. The Maxima SYBR Green/ROX qPCR Master Mix from Thermo was employed for qRT-PCR analysis, with β-actin as the internal reference gene.

Proteomics Analysis: Proteomics analysis was undertaken to examine the hydrogels cocultured in this study. After 7 d of coculture, samples were collected for protein extraction, with three replicates per group. Protein identification and quantification were achieved through reverse-phase high-performance liquid chromatography (Bio-rad, USA). Mass spectrometry data were subjected to both qualitative and quantitative analyses using the MaxQuant/Andromeda software (version 1.3.0.5). Further analyses were performed with various software tools, including DAVID, String, Cytoscape, and OmicStudio. Differentially-expressed proteins were defined as those exhibiting a significance level of $p < 0.05$.

WB Experiments: Cocultured BMSCs were harvested regularly for WB experiments, with total protein extracted using a RIPA lysis buffer (Beyotime). Protein concentrations were determined using a bicinchoninic acid assay kit (Solarbio, Beijing, China). Subsequently, 20 µg of protein from each sample was loaded onto a 10% Sodium sodecyl sulfate polyacrylamide gel electrophoresis gel (New Cell & Molecular, Suzhou, China) and subjected to electrophoresis. Proteins were transferred to membranes, which were then blocked. Membranes were incubated with the primary antibodies anti-TLR4, anti-P65, anti-p-P65, anti-STAT3, anti-p-STAT3, anti-ERK, anti-p-ERK, and Gapdh (all sourced from Abcam). After thorough washing with Tris-buffered saline-Tween (Biosharp), colorimetric detection was carried out using horseradish peroxidase-conjugated secondary antibodies. Protein bands were visualized using an imaging system (Bio-Rad). Quantitative analysis of the proteins was performed using ImageJ.

qRT-PCR of BMDMS In Vitro: BMDMs were cocultured for 7 d and total RNA extracted from cells in each sample utilizing Trizol reagent. The extracted RNA was then subjected to reverse transcription to produce cDNA using a reverse transcription kit from Takara. The MaximaTM SYBR Green/ROX qPCR Master Mix from Thermo Fisher Scientific was employed for qRT-PCR analysis. All reactions were conducted in triplicate, and β-actin was used as the internal reference gene.

Statistical Analysis: Five replicates ($n = 5$) were included for all in vivo animal experiments. Unless otherwise specified, triple replicates ($n = 3$) were studied in other experiments. All experimental data are expressed as mean ± standard deviation. Statistical analyses and graphical representation were conducted using GraphPad Prism or Origin software. Group comparisons were assessed through one-way or two-way analysis of variance, followed by Tukey's multiple comparison test. Statistical significance is represented as * for $p < 0.05$, ** for $p < 0.01$, *** for $p < 0.001$, and **** for $p < 0.0001$. Nonsignificant differences are indicated by "ns."

Supporting Information

Supporting Information is available from the Wiley Online Library or from the author.

Acknowledgements

J.W., L.Z., and L.W. contributed equally to this work. The work was supported by the National Natural Science Foundation of China (Nos. 82072438, 82272501, 82120108017, 82102589, and 82302683), Natural Science Foundation of Jiangsu Province (No. BK20211504), Natural Science Foundation of Beijing (No. 7222031), Social Development Project of Jiangsu Province (No. BE2021646), Jiangsu Province "333 Project" Talent Project (No. 2069999), and the Suzhou Gusu Health Talent Program (Nos. GSWS2021009, GSWS2020001, and GSWS2021007).

Conflict of Interest

The authors declare no conflict of interest.

Data Availability Statement

The data that support the findings of this study are available from the corresponding author upon reasonable request.

Keywords

bletilla striata polysaccharides, bone regeneration, hydrogels, macrophages, mesoporous bioactive glass

Received: November 5, 2023
Revised: January 5, 2024
Published online: January 19, 2024

[1] R. Dimitriou, E. Jones, D. McGonagle, P. V. Giannoudis, *BMC Med.* **2011**, *9*, 66.
[2] J. Li, X. Jiang, H. Li, M. Gelinsky, Z. Gu, *Adv. Mater.* **2021**, *33*, 2004172.
[3] T. U. Luu, S. C. Gott, B. W. Woo, M. P. Rao, W. F. Liu, *ACS Appl. Mater. Interfaces* **2015**, *7*, 28665.
[4] a) J. Wang, S. Qian, X. Liu, L. Xu, X. Miao, Z. Xu, L. Cao, H. Wang, X. Jiang, *J. Mater. Chem. B* **2017**, *5*, 3364; b) M. Locati, G. Curtale, A. Mantovani, *Annu. Rev. Pathol.* **2020**, *15*, 123.
[5] a) J. L. Sun, K. Jiao, L. N. Niu, Y. Jiao, Q. Song, L. J. Shen, F. R. Tay, J. H. Chen, *Biomaterials* **2017**, *113*, 203; b) C. Shi, E. G. Pamer, *Nat. Rev. Immunol.* **2011**, *11*, 762.
[6] a) X. Li, X. T. He, Y. Yin, R. X. Wu, B. M. Tian, F. M. Chen, *J. Cell Mol. Med.* **2017**, *21*, 3162; b) P. Xiao, X. Han, Y. Huang, J. Yang, L. Chen, Z. Cai, N. Hu, W. Cui, W. Huang, *Bioact. Mater.* **2024**, *32*, 242.
[7] X. Wang, G. Wang, S. Zingales, B. Zhao, *Tissue Eng., Part B* **2018**, *24*, 463.
[8] b) Q. Zhang, X. Wang, G. Kuang, Y. Yu, Y. Zhao, *Research* **2022**, *2022*, 9784510; b) Z. Xu, L. Wu, Y. Tang, K. Xi, J. Tang, Y. Xu, J. Xu, J. Lu, K. Guo, Y. Gu, L. Chen, *Adv. Healthcare Mater.* **2023**, *12*, e2201661.
[9] P. Yang, Y. Ju, X. Liu, Z. Li, H. Liu, M. Yang, X. Chen, L. Lei, B. Fang, *Mater. Today Bio.* **2023**, *23*, 100875.
[10] a) R.-S. Hsu, P.-Y. Chen, J.-H. Fang, Y.-Y. Chen, C.-W. Chang, Y.-J. Lu, S.-H. Hu, *Adv. Sci.* **2019**, *6*, 1900520; b) L. Yang, L. Fan, X. Lin, Y. Yu, Y. Zhao, *Adv. Sci.* **2023**, *10*, e2304190; c) L. Yang, W. Yang, W. Xu, Y. Zhao, L. Shang, *Chem. Eng. J.* **2023**, *476*, 146797.
[11] a) H. Wang, M. B. Hansen, D. W. P. M. Loewik, J. C. M. van Hest, Y. Li, J. A. Jansen, S. C. G. Leeuwenburgh, *Adv. Mater.* **2011**, *23*, H119; b) Z. Mu, K. Chen, S. Yuan, Y. Li, Y. Huang, C. Wang, Y. Zhang, W. Liu, W. Luo, P. Liang, X. Li, J. Song, P. Ji, F. Cheng, H. Wang, T. Chen, *Adv. Healthcare Mater.* **2020**, *9*, 19014; c) P. Yang, Y. Ju, X. Liu, Z. Li, H. Liu, M. Yang, X. Chen, L. Lei, B. Fang, *Mater. Today Bio.* **2023**, *23*, 100875.
[12] J. Tang, K. Xi, H. Chen, L. Wang, D. Li, Y. Xu, T. Xin, L. Wu, Y. Zhou, J. Bian, Z. Cai, H. Yang, L. Deng, Y. Gu, W. Cui, L. Chen, *Adv. Funct. Mater.* **2021**, *31*, 2102465.
[13] X. Zhan, L. Jia, Y. Niu, H. Qi, X. Chen, Q. Zhang, J. Zhang, Y. Wang, L. Dong, C. Wang, *Biomaterials* **2014**, *35*, 10046.
[14] a) Z. Chen, L. Cheng, Y. He, X. Wei, *Int. J. Biol. Macromol.* **2018**, *120*, 2076; b) Y. Wang, S. Han, R. Li, B. Cui, X. Ma, X. Qi, Q. Hou, M. Lin, J. Bai, S. Li, *Int. J. Biol. Macromol.* **2019**, *122*, 628; c) J. Pajarinen, T. Lin, E. Gibon, Y. Kohno, M. Maruyama, K. Nathan, L. Lu, Z. Yao, S. B. Goodman, *Biomaterials* **2019**, *196*, 80.
[15] a) A. Hoppe, N. S. Gueldal, A. R. Boccaccini, *Biomaterials* **2011**, *32*, 2757; b) D. S. Brauer, *Angew. Chem., Int. Ed. Eng.* **2015**, *54*, 4160; c) Y. Zhou, C. Wu, J. Chang, *Mater. Today* **2019**, *24*, 41.
[16] Q. Zhang, G. Kuang, Y. Yu, X. Ding, H. Ren, W. Sun, Y. Zhao, *ACS Appl. Mater. Interfaces* **2022**, *14*, 48527.
[17] a) L. Yang, X. Wang, Y. Yu, L. Shang, W. Xu, Y. Zhao, *Nano Res.* **2023**, *16*, 5292; b) N. Alasvand, A. Behnamghader, P. B. Milan, S. Simorgh, A. Mobasheri, M. Mozafari, *Mater. Today Bio.* **2023**, *20*, 100647.
[18] a) Y. Luo, H. Diao, S. Xia, L. Dong, J. Chen, J. Zhang, *J. Biomed. Mater. Res., Part A* **2010**, *94A*, 193;
[19] F. Hou, W. Jiang, Y. Zhang, J. Tang, D. Li, B. Zhao, L. Wang, Y. Gu, W. Cui, L. Chen, *Chem. Eng. J.* **2022**, *427*, 132000.
[20] T. Xin, Y. Gu, R. Cheng, J. Tang, Z. Sun, W. Cui, L. Chen, *ACS Appl. Mater. Interfaces* **2017**, *9*, 41168.
[21] Y. Zhang, Z. Zhi, T. Jiang, J. Zhang, Z. Wang, S. Wang, *J. Controlled Release* **2010**, *145*, 257.
[22] a) V. Karageorgiou, D. Kaplan, *Biomaterials* **2005**, *26*, 5474; b) S. Saravanan, R. S. Leena, N. Selvamurugan, *Int. J. Biol. Macromol.* **2016**, *93*, 1354.
[23] D. F. Farrar, *Int. J. Adhes. Adhes.* **2012**, *33*, 89.
[24] M. Zhang, H. An, Z. Gu, Z. Huang, F. Zhang, Y. Wen, P. Zhang, *Adv. Mater.* **2023**, *35*, 2212258.
[25] E. Safwat, M. L. Hassan, S. Saniour, D. Y. Zaki, M. Eldeftar, D. Saba, M. Zazou, *J. Biomater. Appl.* **2018**, *32*, 1371.
[26] L. Quan, Y. Xin, X. Wu, Q. Ao, *Polymers* **2022**, *14*, 2184.
[27] H. Cui, W. Zhu, B. Holmes, L. G. Zhang, *Adv. Sci.* **2016**, *3*, 1600058.
[28] J. Wu, Z. Pan, Z.-Y. Zhao, M.-H. Wang, L. Dong, H.-L. Gao, C.-Y. Liu, P. Zhou, L. Chen, C.-J. Shi, Z.-Y. Zhang, C. Yang, S.-H. Yu, D.-H. Zou, *Adv. Mater.* **2022**, *34*, 2200115.
[29] K. Zheng, W. Niu, B. Lei, A. R. Boccaccini, *Acta Biomater.* **2021**, *133*, 168.
[30] F. Loi, L. A. Cordova, J. Pajarinen, T.-h. Lin, Z. Yao, S. B. Goodman, *Bone* **2016**, *86*, 119.
[31] a) L. Claes, S. Recknagel, A. Ignatius, *Nat. Rev. Rheumatol* **2012**, *8*, 133; b) P. J. Harwood, J. B. Newman, A. L. J. O. Michael, *Trauma* **2010**, *24*, 9.
[32] Y. Niu, Q. Li, R. Xie, S. Liu, R. Wang, P. Xing, Y. Shi, Y. Wang, L. Dong, C. Wang, *Biomaterials* **2017**, *139*, 39.
[33] F. Y. McWhorter, T. Wang, N. Phoebe, C. Thanh, W. F. Liu, *Proc. Nat. Acad. Sci. USA* **2013**, *110*, 17253.
[34] O. Bastian, J. Pillay, J. Alblas, L. Leenen, L. Koenderman, T. Blokhuis, *J. Leukocyte Biol.* **2011**, *89*, 669.
[35] L. Vi, G. S. Baht, H. Whetstone, A. Ng, Q. Wei, R. Poon, S. Mylvaganam, M. Grynpas, B. A. Alman, *J. Bone Miner. Res.* **2015**, *30*, 1090.
[36] a) F. Belema-Bedada, S. Uchida, A. Martire, S. Kostin, T. Braun, *Cell Stem Cell* **2008**, *2*, 566; b) A. Mantovani, A. Sica, S. Sozzani, P. Allavena, A. Vecchi, M. Locati, *Trends Immunol.* **2004**, *25*, 677.
[37] a) L. Gong, Y. Zhao, Y. Zhang, Z. Ruan, *Ann. Clin. Lab. Sci.* **2016**, *46*, 65; b) Y. Zhang, T. Boese, R. E. Unger, J. A. Jansen, C. J. Kirkpatrick, J. J. J. P. van den Beucken, *Cell Tissue Res.* **2017**, *369*, 273.
[38] a) N. Vanrooijen, A. Sanders, *J. Immunol. Methods* **1994**, *174*, 83; b) Y. Zhu, Z. Ma, L. Kong, Y. He, H. F. Chan, H. Li, *Biomaterials* **2020**, *256*, 120216.
[39] Y.-Y. Wang, H. Jiang, J. Pan, X.-R. Huang, Y.-C. Wang, H.-F. Huang, K.-F. To, D. J. Nikolic-Paterson, H.-Y. Lan, J.-H. Chen, *J. Am. Soc. Nephrol.* **2017**, *28*, 2053.
[40] a) K. A. Alexander, M. K. Chang, E. R. Maylin, T. Kohler, R. Mueller, A. C. Wu, N. Van Rooijen, M. J. Sweet, D. A. Hume, L. J. Raggatt, A. R. Pettit, *J. Bone Miner. Res.* **2011**, *26*, 1517; b) P. Guihard, Y. Danger, B. Brounais, E. David, R. Brion, J. Delecrin, C. Richards, S. Chevalier, F. Redini, D. Heymann, H. Gascan, F. Blanchard, *Bone* **2012**, *50*, S83.
[41] X. Niu, J. Yu, Q. Huang, J. Yu, Y. Yang, H. Song, Y. Liu, X. Xiao, L. Cui, W. Li, *Autoimmunity* **2022**, *55*, 650.